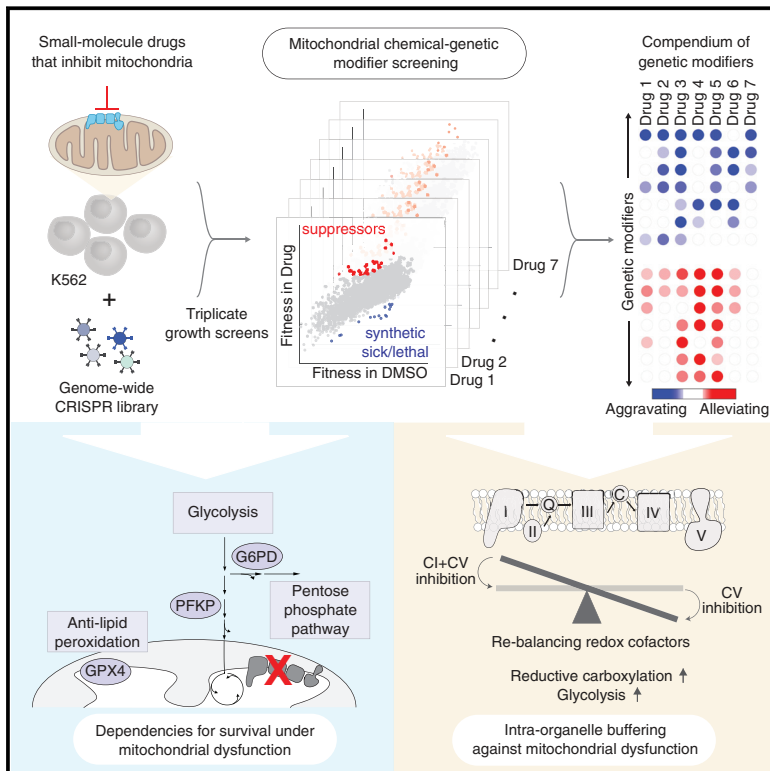


A Compendium of Genetic Modifiers of Mitochondrial Dysfunction Reveals Intra-organelle Buffering

Graphical Abstract



Authors

Tsz-Leung To, Alejandro M. Cuadros, Hardik Shah, ..., Stuart L. Schreiber, Scott B. Vafai, Vamsi K. Mootha

Correspondence

vamsi@hms.harvard.edu

In Brief

A chemical-genetic map of the mitochondrion provides insights into the pathways that modulate its function.

Highlights

- Genome-wide CRISPR screens were performed with multiple mitochondrial inhibitors
- Loss of *G6PD*, *PFKP*, or *GPX4* is synthetic lethal with mitochondrial dysfunction
- “Intra-mitochondrial” interactions are pervasive
- Fitness defect from CV inhibition is alleviated by simultaneous loss of CI activity



A Compendium of Genetic Modifiers of Mitochondrial Dysfunction Reveals Intra-organelle Buffering

Tsz-Leung To,¹ Alejandro M. Cuadros,¹ Hardik Shah,^{1,2,3} Wendy H.W. Hung,¹ Yang Li,^{1,2,3} Sharon H. Kim,^{1,2,3} Daniel H.F. Rubin,^{1,2,3} Ryan H. Boe,¹ Sneha Rath,^{1,2,3} John K. Eaton,¹ Federica Piccioni,¹ Amy Goodale,¹ Zohra Kalani,¹ John G. Doench,¹ David E. Root,¹ Stuart L. Schreiber,^{1,2,4} Scott B. Vafai,^{1,5} and Vamsi K. Mootha^{1,2,3,5,6,*}

¹Broad Institute of Harvard and MIT, Cambridge, MA 02142, USA

²Howard Hughes Medical Institute, Massachusetts General Hospital, Boston, MA 02114, USA

³Department of Molecular Biology, Massachusetts General Hospital, Boston, MA 02114, USA

⁴Department of Chemistry and Chemical Biology, Harvard University, Cambridge, MA 02138, USA

⁵Senior author

⁶Lead Contact

*Correspondence: vamsi@hms.harvard.edu

<https://doi.org/10.1016/j.cell.2019.10.032>

SUMMARY

Mitochondrial dysfunction is associated with a spectrum of human conditions, ranging from rare, inborn errors of metabolism to the aging process. To identify pathways that modify mitochondrial dysfunction, we performed genome-wide CRISPR screens in the presence of small-molecule mitochondrial inhibitors. We report a compendium of chemical-genetic interactions involving 191 distinct genetic modifiers, including 38 that are synthetic sick/lethal and 63 that are suppressors. Genes involved in glycolysis (PFKP), pentose phosphate pathway (G6PD), and defense against lipid peroxidation (GPX4) scored high as synthetic sick/lethal. A surprisingly large fraction of suppressors are pathway intrinsic and encode mitochondrial proteins. A striking example of such “intra-organelle” buffering is the alleviation of a chemical defect in complex V by simultaneous inhibition of complex I, which benefits cells by rebalancing redox cofactors, increasing reductive carboxylation, and promoting glycolysis. Perhaps paradoxically, certain forms of mitochondrial dysfunction may best be buffered with “second site” inhibitors to the organelle.

INTRODUCTION

Defects in mitochondrial function accompany a spectrum of conditions, ranging from rare inborn errors of metabolism to the aging process itself. To date, nearly 300 rare, monogenic forms of mitochondrial disease have been identified (Frazier et al., 2019)—each presenting typically in a devastating manner with tissue-specific pathology—making these disorders a very common collection of inborn errors of metabolism. Mitochondrial disorders typically present in a devastating manner during childhood with tissue-specific pathology, and there are no

proven effective therapies available. Many common diseases, including Parkinson’s disease and type 2 diabetes, are also characterized by mitochondrial dysfunction, though an important question is whether organelle dysfunction is a cause or consequence of end pathology (Vafai and Mootha, 2012). A quantitative decline in mitochondrial abundance and activity has emerged as a signature of the aging process across different organisms (Trounce et al., 1989; Zahn et al., 2007).

How mitochondrial defects lead to such pleiotropic and heterogeneous pathologies is a major unsolved problem, and addressing this problem is challenging for several reasons. First, the organelle is highly complex, housing numerous coupled metabolic pathways that tend to be densely interconnected. Lesions at different points within the same mitochondrial pathway can often have highly non-uniform biochemical consequences. For example, defects in complex I and III both cause a decline in ATP production by oxidative phosphorylation (OXPHOS) but have opposite effects on *de novo* pyrimidine biosynthesis (Shaham et al., 2010). Second, the organelle’s machinery is coupled, often with redundancy, to metabolic and regulatory pathways in other cellular compartments. For example, in cultured cells, glycolysis is capable of compensating for ATP production from OXPHOS as long as glucose is provided in the media. Third, mitochondrial dysfunction can activate stress responses (Bao et al., 2016), which in some instances buffer against toxicity while in other instances serve as an effector of end pathology. Fourth, non-linear feedback loops help to ensure energetic and redox homeostasis acutely in response to stressors and over long-term, adaptive timescales (Balaban et al., 1986; Chance and Williams, 1955; Cogliati et al., 2013). It is clear that genetic networks support mitochondrial function and can buffer against or contribute to pathology. However, these networks have not been systematically mapped.

Genetic modifier screening on a sensitized chemical background presents a powerful means to decipher cellular networks (Hillenmeyer et al., 2008). Inspired by the concept of genetic interactions, the goal of such “chemical-genetics” approaches is to compare the combined effects of a genetic perturbation and



a chemical insult. Such approaches can help to reveal genetic circuitry centered on the targets of well-studied drugs. While genome-wide chemical-genetic approaches have been applied extensively in yeast, the technology has only recently become available to extend these approaches to mammalian cells (Hart et al., 2015; Shalem et al., 2014; Wang et al., 2014). Recently, several studies have showcased the power of targeted CRISPR screening (Birsoy et al., 2015) and even genome-scale CRISPR screening (Arroyo et al., 2016) in mammalian cells to uncover new aspects of mitochondrial biology. The genome-scale CRISPR approach has even helped to nominate hypoxia as a novel and seemingly counterintuitive therapeutic approach for mitochondrial dysfunction (Jain et al., 2016). As these studies demonstrated, genome-scale approaches afford the opportunity to identify cellular pathways operating inside or outside of mitochondria that control the organelle, without prior assumptions of the nature of interactors.

Here, we report the creation of a genome-scale compendium of chemical-genetic interactions focused on mitochondrial biology. We use a collection of mitochondrial inhibitors that allows us to model distinct, canonical modes of “mitochondrial dysfunction,” including defects in replication and translation of the mtDNA, defects in individual complexes of the electron transport chain, impaired ATP formation by OXPHOS via the F1Fo-ATPase, and deficits in membrane potential polarization. We perform genome-wide CRISPR screens in triplicate to identify chemical-genetic interactions that are either synthetic sick/lethal or alleviating. We report a compendium of chemical-genetic interactions involving 191 distinct nuclear genes. These interactions fall into different categories, including genetic modifiers that suppress mitochondrial dysfunction as well as those that aggravate it. About 65% of these modifiers themselves encode mitochondrial-localized proteins underscoring dense connectivity within the organelle. We illustrate how our resource can be useful by reporting four key results, including the surprising finding that the loss of complex I activity (genetically or with drugs such as metformin or piericidin) is capable of suppressing cellular defects stemming from chemical inhibition of complex V.

RESULTS

Genome-wide CRISPR Modifier Screens in the Presence of Mitochondrial Inhibitors

To systematically uncover genetic pathways that aggravate or suppress mitochondrial dysfunction, we combined genome-wide CRISPR growth screening on sensitized backgrounds in which mitochondrial physiology is inhibited at distinct nodes (Figure 1A). We modeled mitochondrial dysfunction using small molecule inhibitors that target distinct aspects of mitochondrial physiology: respiratory chain complex I (piericidin), complex III (antimycin), complex V (oligomycin), mitochondrial membrane potential (antimycin+oligomycin), mitochondrial DNA replication (ethidium bromide), and mitochondrial protein translation (chloramphenicol). We also included metformin, whose proposed targets include complex I (Owen et al., 2000; Wheaton et al., 2014) but may include other targets as well (Madiraju et al., 2014). We chose the minimal drug concentrations that were sufficient to blunt OXPHOS activity in K562 cells (see the legend of Figure 1B

for drug doses) while allowing cell proliferation. We confirmed complete OXPHOS inhibition by the observation of massive cell death in galactose but not glucose (Arroyo et al., 2016) in K562 cells (Figure S1A). We observed a high dosage requirement for metformin to inhibit respiration (Figure S1B), consistent with what has been seen in prior studies (Wheaton et al., 2014). In addition, we confirmed the efficacy of ethidium bromide in depleting mtDNA (Figure S1C), chloramphenicol in inhibition of mitochondrial translation (Figure S1D), and antimycin+oligomycin in collapsing membrane potential (Figure S1E).

We performed genome-wide CRISPR modifier screens in biological triplicate in K562 cells using an optimized single guide RNA (sgRNA) library (Doench et al., 2016) (Figure 1B). Cells were split and treated with DMSO or one of seven different drug treatments 7 days after infection and cultured for an additional 15 days in media containing high glucose (25 mM), pyruvate, and uridine. To proliferate, cells lacking a functional electron transport chain are dependent on glucose to fuel high glycolytic activity for ATP generation, exogenous pyruvate for recycling NADH into NAD⁺ through lactate dehydrogenase, and exogenous uridine for pyrimidine salvage (King and Attardi, 1989; Morais et al., 1980). The sgRNAs were PCR amplified from the genomic DNA of harvested cells. Next-generation sequencing was performed, and the abundance of each sgRNA in the drug treatment on day 15 was compared to the day 0 baseline. The growth curves for cumulative differences show moderate growth defects—i.e., slower but steady proliferation—in cells under metformin, piericidin, antimycin, and chloramphenicol (Figure 1C). On the other hand, oligomycin, antimycin+oligomycin, and ethidium bromide treatments appear to impact proliferation more significantly (Figure 1C). The growth curves demonstrate consistent effects of each drug across the biological triplicates. Of note, two of our “day 15 samples,” one for DMSO and one for metformin, were lost during the PCR step, yielding a total of 22 (out of 24) successful 15-day screens (Table S2).

Of the 19,000 genes targeted by our CRISPR library, 11,102 genes are expressed in K562 cells (Table S1; STAR Methods) and could be scored for their chemical-genetic interactions (Figure 1D). By comparing the fitness of a gene’s loss in the presence of a drug (Z_{drug}) to the fitness of that same gene’s loss in the absence of a drug (Z_{DMSO}), we can define the relative fitness of a knockout (KO) in drug versus DMSO simply as $\Delta Z_{\text{Drug}} = (Z_{\text{Drug}} - Z_{\text{DMSO}}) / \sqrt{2}$ (see Table S1; STAR Methods). We classify 38 hits as “synthetic sick/lethal” with $\Delta Z_{\text{Drug}} < -2.4$ and 154 genes as “buffering” with $\Delta Z_{\text{Drug}} > 4.8$ (we use a higher threshold on this side of the screen, since in a growth screen, KOs are much more likely to be depleted by chance alone than enriched because of drop outs). Among the 154 genes involved in buffering interactions, we find that a subset of 63 genes are additionally enriched on day 15 as compared with baseline on day 0 (i.e., $Z_{\text{Drug}} > 2.4$). These 63 genetic modifiers with proliferative advantages are termed “suppressors,” whereas the other 91 are characterized as “epistatic buffering” (Figure 1D), a term that is used to describe an interaction between two deleterious effects (Jasnos and Korona, 2007). Of note, only loss of *CYC1* (complex III component) shows opposing effects in two treatments—it aggravates antimycin+oligomycin but epistatically buffers (without alleviating) oligomycin. To buttress the above analysis pipeline,

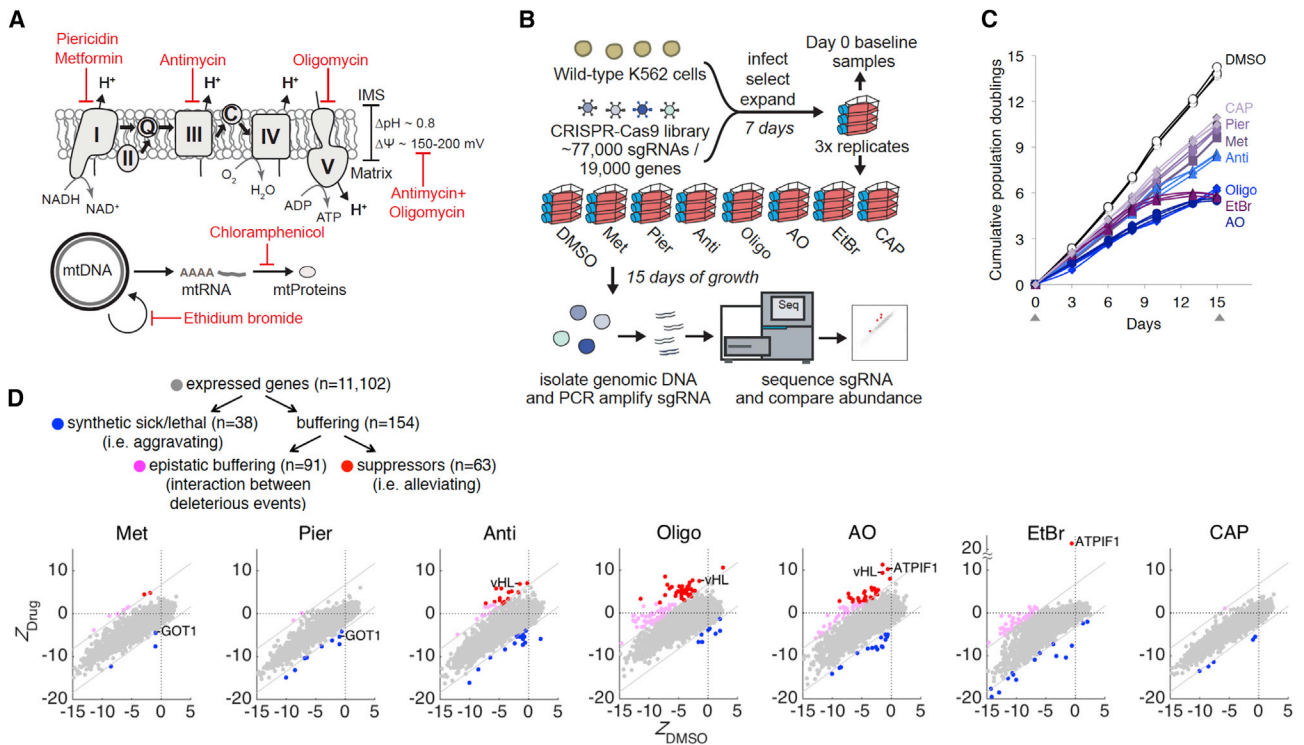


Figure 1. Genome-wide CRISPR Screens to Identify Modifiers of Mitochondrial Dysfunction

(A) Mitochondrial chemical inhibitors used in this study: piericidin (complex I), antimycin (complex III), oligomycin (complex V), antimycin+oligomycin ($\Delta\Psi_m$), ethidium bromide (mitochondrial DNA replication), chloramphenicol (mitochondrial translation), and metformin (complex I is among the proposed targets).

(B) Schematic overview of the genome-wide CRISPR screens in K562 cells. The following drug dosages were used: 0.1% DMSO, 10 mM metformin (Met), 10 nM piericidin (Pier), 100 nM antimycin (Anti), 10 nM oligomycin (Oligo), 10 nM antimycin + 10 nM oligomycin (AO), 100 ng/mL ethidium bromide (EtBr), and 10 μ g/mL chloramphenicol (CAP).

(C) Growth curves for cumulative differences in growth under drug treatments. Growth curves for individual replicates over 15 days are shown. Gray arrows denote time points at which samples were harvested.

(D) Categories of genetic interactions and the number of genetic modifiers associated with each category. Scatterplots of Z scores showing knockouts (KOs) that are enriched or depleted in each drug versus DMSO are shown. KOs are scored by $\Delta Z_{Drug} = (Z_{Drug} - Z_{DMSO})/\sqrt{2}$ (see STAR Methods). KO enrichment (shown in red or magenta, $\Delta Z_{Drug} > 4.8$) and depletion (shown in blue, $\Delta Z_{Drug} < -2.4$) are used to define buffering and synthetic sick/lethal interactions, respectively. Among buffering interactions, suppressors ($Z_{Drug} > 2.4$) are shown in red. Known genetic modifiers (*vHL* and *ATP1F1* as genetic suppressors of OXPHOS inhibitors and *GOT1* loss as aggravator) are highlighted. The gray dotted lines represent the cutoffs for interactions.

See also Figure S1.

we independently scored the genes using the model-based MAGECK algorithm (Li et al., 2014) (Table S1; STAR Methods). The results from MAGECK are highly consistent with the ΔZ_{Drug} scores. The fact that two different data analysis methods arrive largely at the same “hits” indicates that our results are not sensitive to the analysis type.

Of the 38 distinct synthetic sick/lethal hits that aggravate mitochondrial dysfunction, 23 (61%) interact with only one drug, and 15 (39%) have interactions shared by multiple drugs (Figure 2A). Of the 63 distinct suppressors, 31 (49%) interact with only one drug, and 32 (51%) have interactions shared by multiple drugs (Figure 2B). Importantly, the synthetic sick/lethal hits and suppressors are considered candidate genetic modifiers until proven in targeted experiments outside the context of a pooled screen.

Four observations suggest the robustness of the screening results. First, the guide counts between biological replicates are well correlated as visualized by principal-component analysis (Figure S1F). Second, the negative-controls guides (1,000 non-

targeting sgRNAs and sgRNAs for 3,726 non-expressed genes in K562) remain tightly distributed over the course of the screens among all treatments, whereas the guides for the core essential genes (Hart et al., 2015) are, as expected, strongly depleted at the endpoint (day 15) of the screen (Figure S1G; Table S3). Third, we recover the three published human mitochondrial chemical-genetic interactions, including those that involve *vHL* (Jain et al., 2016), *ATP1F1* (Chen et al., 2014), and *GOT1* (Birsoy et al., 2015) (Figure 1D). Fourth, we validated newly identified aggravating and buffering interactions in targeted experiments (Figures 3–6).

Among the treatments that lead to a more severe growth defect, reduced depletion of sgRNAs targeting essential genes might represent an artifact. That is, sgRNAs may have depleted more in DMSO than in the drug samples simply due to a large difference in growth rates, which would be misidentified as epistatic buffering interactions under the drug. However, it is unlikely the case as (1) drugs that lead to severe growth defect

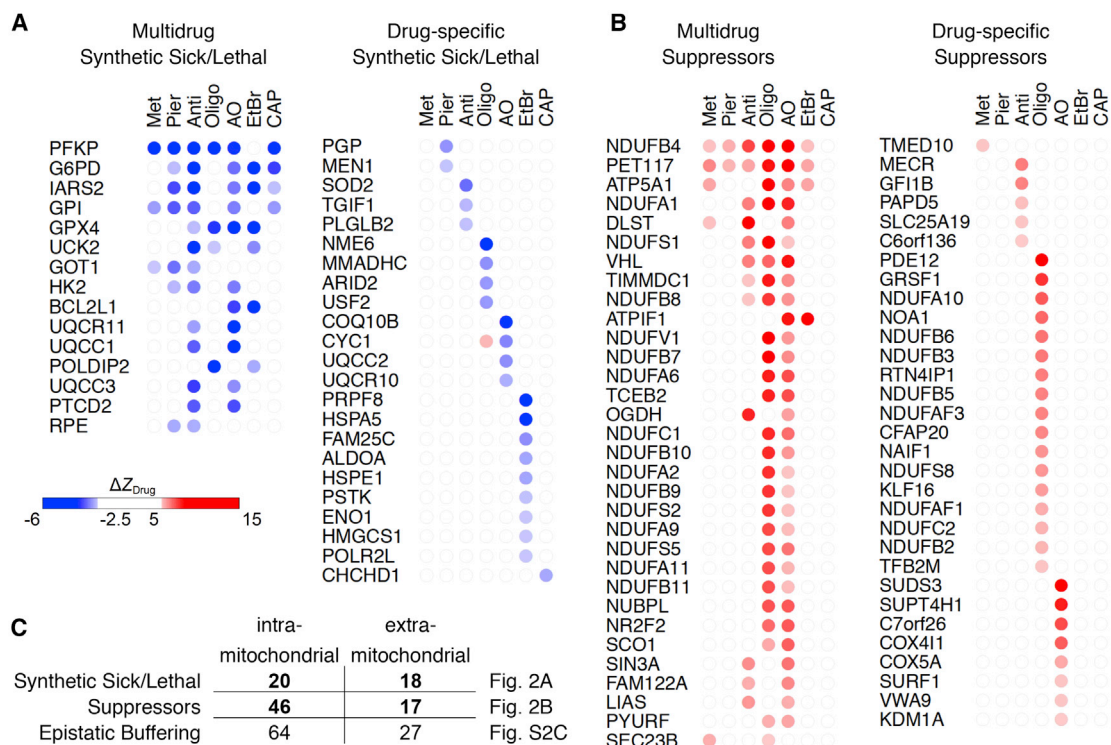


Figure 2. Genetic Modifiers of Distinct Modes of Mitochondrial Dysfunction

(A) The 38 synthetic sick/lethal hits that score in ≥ 1 drug ($\Delta Z_{Drug} < -2.4$).

(B) The 63 suppressors that score in ≥ 1 drug ($\Delta Z_{Drug} > 4.8$, and $Z_{Drug} > 2.4$).

For (A) and (B), genes are further divided into two panels. The left panel contains genes that have interactions with multiple drugs and is ordered by the number of drugs under which interactions occur. The right panel contains genes with only drug-specific interactions, and genes are listed by the specific drug and ordered by the strength of interaction. Gene-drug pairs that do not score are colored white ($-2.4 \leq \Delta Z_{Drug} \leq 4.8$).

(C) Counts of modifiers that are implicated in intra-mitochondrial versus extra-mitochondrial interactions.

See also Figure S2. The expected fraction of "intra-mitochondrial" in each category is 6%, as only 6% of all nuclear genes encode mitochondrial proteins.

(oligomycin, antimycin+oligomycin, and ethidium bromide) have a large number of unique genetic interactions (Figure S2A), and (2) generally essential genes, such as those encoding the cytosolic translation machinery, are not buffered under severe growth defect (Figure S4D). This is in stark contrast with genes that encode the mitochondrial translation machinery, which are significantly buffered under oligomycin and ethidium bromide treatment (Figure S4D).

Of the drugs we tested, metformin is of notable interest since it is one of the most widely used drugs in the world to treat type 2 diabetes and is now in clinical trials for aging (Barzilai et al., 2016), yet its direct target(s) of action is still debated. Classical studies have clearly demonstrated that complex I is a target (Owen et al., 2000), but there may be additional sites of action (Madiraju et al., 2014). Piericidin and metformin are the most similar with respect to their genome-wide profiles across the battery of drugs we tested (Figures S1F and S2A), consistent with complex I being a target of metformin.

Intra-mitochondrial Chemical-Genetic Interactions Are Pervasive

All of the chemicals used in this screen have targets localized within mitochondria (Figure 1A), and hence we can classify chem-

ical-genetic interactions as "intra-mitochondrial" if the identified genetic modifier encodes a mitochondrial protein or "extra-mitochondrial" if the identified genetic modifier encodes a protein localized outside of mitochondria. Of the 38 synthetic sick/lethal hits (Figure 2A), 20 (53%) are involved in intra-mitochondrial interactions. Of the 63 suppressors (Figure 2B), 46 (73%) are involved in intra-mitochondrial interactions. Of the 91 epistatic buffering hits (Figure S2C), 64 (70%) are involved in intra-mitochondrial interactions (Figure 2C). As genes encoding mitochondrial proteins only account for 6% of the human proteome (Calvo et al., 2016), intra-mitochondrial interactions are dramatically overrepresented among both synthetic sick/lethal hits (Fisher $p = 3.5 \times 10^{-15}$) and suppressors (Fisher $p = 8.2 \times 10^{-43}$). The overrepresentation of genes encoding mitochondrial proteins among epistatic buffering interactions could be a consequence of the fact that gene losses are redundant with chemical inhibition of the same target. The rationale for overrepresentation of intra-mitochondrial interactions among synthetic sick/lethal hits and suppressors is not obvious, and such interactions may point to dense functional connectivity that occurs inside the organelle, consistent with global yeast genetic interaction screens, where functionally related genes tend to show genetic interactions (Costanzo et al., 2016; Hoppins et al., 2011).

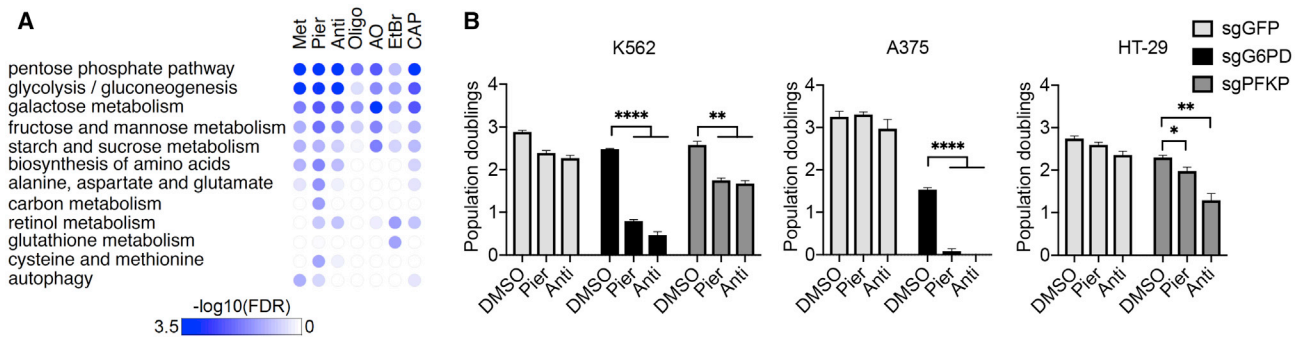


Figure 3. Losses of Genes Involved in Glycolysis or Pentose Phosphate Pathway Are Synthetic Sick/Lethal with OXPPOS Dysfunction

(A) Top categories of Kyoto Encyclopedia of Genes and Genomes (KEGG) pathways among depleted KOs by gene set enrichment analysis (GSEA). The 11,102 genes was ranked by ΔZ_{Drug} in descending order, and GSEA was run in the negative mode. Pathways are ordered by the maximum of $-\log_{10}$ false discovery rate (FDR) across 7 drugs.

(B) Growth phenotypes of K562, A375, or HT-29 cells with sgRNAs directed against the genes indicated under piericidin or antimycin treatment. Cell counts were performed 3 days post drug treatment (average \pm SEM, $n = 3$). * $p < 0.05$, ** $p < 0.01$, or **** $p < 0.0001$ indicates two-tailed Student's *t* test *p* value.

Genes Whose Loss Aggravates the Toxic Effects of Mitochondrial Inhibitors

We identify 38 unique genes whose loss aggravates growth defects for ≥ 1 mitochondrial inhibitor (Figure 2A); i.e., they are synthetic sick or lethal with mitochondrial dysfunction. As expected, we recovered *GOT1*, which has previously been identified to be essential for growth under phenformin treatment (Birsoy et al., 2015). Here, we report the chemical-context specificity of this interaction, as *GOT1* loss is aggravated by piericidin and antimycin, but not by the other drugs. Pathway analysis (Figure 3A; Table S4) identifies glycolysis and the pentose phosphate pathway as being enriched. The top scoring multi-drug synthetic sick/lethal hits are *G6PD* (involved in pentose phosphate) and *PFKP* (glycolysis). *A priori*, genes associated with glycolysis are expected to be essential under OXPPOS inhibition, and we recovered multiple genes involved in this pathway (*GPI*, *ALDOA*, *HK2*, and *PFKP*) or in its regulation (*PGP*) among the aggravators. Two genes in the pentose phosphate pathway (*G6PD* and *RPE*) scored, suggesting an increased demand for NADPH or ribose-5-phosphate in the setting of OXPPOS inhibition.

We validated three of the newly identified synthetic lethal interactions, including *G6PD*, *PFKP*, and *GPX4*, which we focus on next. Loss of *G6PD* or *PFKP* increases toxicity of multiple mitochondrial inhibitors, including piericidin and antimycin, which we validated in multiple cell lines (Figure 3B). *G6PD* deficiency represents one of the most common enzymopathies (Cappellini and Fiorelli, 2008) and is polymorphic in hundreds of millions of individuals worldwide. To our knowledge, the synthetic sick/lethal interaction between *G6PD* loss and mitochondrial dysfunction has not been previously reported. *PFKP* encodes one of the three isozymes of the phosphofructokinase 1 (PFK-1) expressed in human cells. Of note, the loss of the other two isozymes (*PFKM* and *PFKL*) is tolerated under OXPPOS inhibitions, even when all three isozymes are highly expressed in K562 (Table S1).

GPX4, Whose Loss Is Synthetic Lethal, Is Induced by Mitochondrial Dysfunction to Guard against Ferroptosis

Glutathione peroxidase 4 (*GPX4*) scored as one of the strongest hits among our synthetic sick/lethal interactions; loss of this

enzyme enhances the toxicity of antimycin, oligomycin, ethidium bromide, and antimycin+oligomycin (Figure S3A). It is notable that *GPX4*, along with *GOT1*, was among the most upregulated proteins in a previous proteomic profiling study in cells depleted of mtDNA (Bao et al., 2016) (Figure 4A), suggesting they may be induced by OXPPOS dysfunction. *GPX4* is a selenoprotein (Maiorino et al., 1991; Ursini et al., 1985) that reduces lipid hydroperoxides to their corresponding alcohols to prevent accumulation of toxic byproducts such as malondialdehyde and 4-hydroxynonenal (Maiorino et al., 2018), which can lead to ferroptosis (Dixon et al., 2012; Stockwell et al., 2017; Yang et al., 2014). Moreover, therapy-resistant persister cancer cells are susceptible to loss of *GPX4* function, and this vulnerability has been proposed as a target for cancer therapies (Hangauer et al., 2017; Viswanathan et al., 2017).

We confirmed the synthetic lethal interaction between loss of *GPX4* activity and OXPPOS inhibition by oligomycin (where the screening effect was among the strongest), selecting three cell lines (K562, HAP1, and HeLa) capable of tolerating its loss (Figure 4B) (Meyers et al., 2017). In all three cell types tested, we observed a synthetic lethal interaction between oligomycin and *JKE-1674*, a new specific chemical inhibitor that acts by covalently binding the catalytic selenocysteine residue of *GPX4* without eliminating its expression (Eaton et al., 2018) (Figure S3F) and with an efficacy similar to the commonly used *GPX4* inhibitor ML 210 (Figure 4D). We observed that the strong synthetic lethal interaction in K562 requires the cells to be grown in spent medium, as fresh medium only leads to mild growth defects (Figure S3B). We observed steady-state accumulation of lipid hydroperoxides in cells treated with both oligomycin and *GPX4* inhibitor in spent medium (Figure S3C), consistent with the ferroptotic death phenotype. We confirmed an aggravating interaction between *GPX4* KO HAP1 cells (Figure S3D) and oligomycin (Figures 4C and 4D). As expected, ferroptosis suppressors α -tocopherol and ferrostatin-1, but not the pan-caspase inhibitor zVAD-fmk, rescue the fitness defects of *GPX4* KO cells under oligomycin treatment (Figure 4C).

We next sought to rescue this phenotype by re-expressing *GPX4* in KO cells. *GPX4* encodes multiple protein isoforms

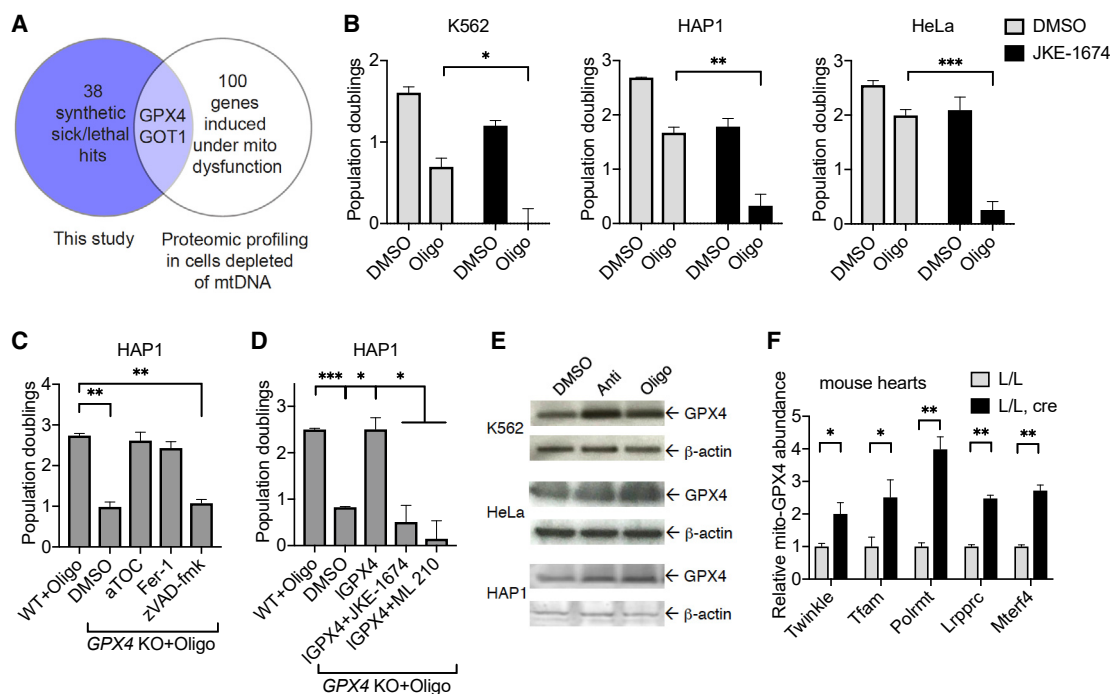


Figure 4. Aggravation of Oligomycin's Toxicity by Loss of GPX4

(A) Venn diagram showing the overlap among the 38 synthetic sick/lethal hits and the 100 most upregulated proteins in a previous proteomic profiling study in cells depleted of mtDNA (Bao et al., 2016).

(B) Growth phenotypes of wild-type cells under a combination of oligomycin and GPX4 inhibition by 10 μ M JKE-1674 for K562 in spent medium, HAP1 in fresh medium, and HeLa in fresh medium. Cell counts were performed 3 days post drug treatment (average \pm SEM, n = 3).

(C) Growth phenotypes of GPX4 KO cells in HAP1 under oligomycin treatment in fresh medium supplemented with ferroptosis inhibitors α -tocopherol (aTOC, 1 μ M), ferrostatin-1 (Fer-1, 1 μ M), or pan-caspase inhibitor zVAD-fmk (1 μ M). Cell counts were performed 3 days post drug treatment (average \pm SEM, n = 3).

(D) Growth phenotypes of GPX4 KO cells in HAP1 under oligomycin with re-expression of IGPX4 or IGPX4 supplemented with the catalytic site-specific GPX4 inhibitors JKE-1674 (10 μ M) or ML 210 (10 μ M) in fresh medium. Cell counts were performed 3 days post treatment (average \pm SEM, n = 2).

(E) Immunoblots for GPX4 and loading control in wild-type K562, HeLa, and HAP1 cells treated with antimycin or oligomycin for 3 days. A representative experiment is shown.

(F) Mitochondrial GPX4 levels derived from a proteomics dataset mitochondrial proteome from the heart tissues of five conditional KO mouse strains with OXPHOS dysfunction (Kühl et al., 2017). The data shown represent the average \pm SEM (n \geq 3). In (B)–(D) and (F), *p < 0.05, **p < 0.01, or ***p < 0.001 indicates two-tailed Student's t test p value.

See also Figure S3.

with distinct subcellular localizations (Savaskan et al., 2007). The two major isoforms, short (sGPX4) and long (IGPX4), are distinguished by the first exon (E1a), which encodes the N-terminal sequences of both isoforms but is truncated in sGPX4 (Figure S3E). The 3' UTR of both isoforms contains a canonical selenocysteine insertion sequence (SECIS) required for GPX4's catalytic activity (Ingold et al., 2018). Using subcellular fractionation (Figure S3F) and microscopy (Figure S3G), we find that IGPX4 is exclusively localized to mitochondria, whereas the sGPX4 is primarily localized in the cytosol. Of note, our subcellular fractionation result and a previous study in mice (Liang et al., 2009) indicate that sGPX4 can also be targeted to the mitochondria. Re-expression of the mitochondria-specific IGPX4 in GPX4 KO cells is sufficient to fully rescue the synthetic lethal interaction with oligomycin in a way that could be inhibited with JKE-1674 or ML 210 (Figure 4D). These experiments demonstrate that GPX4 activity within mitochondria is sufficient to rescue the synthetic lethal interaction, thus providing support for mitochondria being

an important site for lipid hydroperoxide accumulation and ferroptosis under OXPHOS inhibition. These results also implicate an “intra-mitochondrial” synthetic lethal interaction between GPX4 loss and oligomycin toxicity.

Given that GPX4 loss is synthetic lethal with OXPHOS inhibition and previous proteomics analysis (Figure 4A), we asked whether GPX4 expression might rise in response to mitochondrial dysfunction as an adaptive response. Total GPX4 protein was upregulated under oligomycin treatment in K562, HeLa, and HAP1 cells (Figure 4E). To evaluate whether upregulation of GPX4 in response to OXPHOS dysfunction occurs *in vivo*, we re-analyzed the published mitochondrial proteomes from the heart tissues of five different genetic KO models of mitochondrial disease (Kühl et al., 2017) spanning defects in mtDNA replication (*Twinkle*), mtDNA maintenance (*Tfam*), mtDNA transcription (*Polrmt*), mt-mRNA stability and maturation (*Lrpprc*), and mitochondrial transcription termination (*Mterf4*). In all five models of mitochondrial disease, mitochondrial-localized

GPX4 protein levels are increased (Figure 4F), providing strong evidence that mitochondrial GPX4 is induced in response to OXPHOS mitochondrial dysfunction *in vivo*. By showing that GPX4 is inducible in multiple cell types and tissues in the face of OXPHOS inhibition, and that its targeted expression within mitochondria can confer protection against OXPHOS inhibition, we propose GPX4 as an adaptive component for survival under OXPHOS dysfunction.

Genes Whose Loss Is Epistatically Buffered by Mitochondrial Inhibitors

Among the 154 genes involved in buffering interactions (i.e., $\Delta Z_{\text{Drug}} > 4.8$), the majority (91) of gene KOs show no growth advantage in the primary screen as compared with the wild-type cells under drug treatment, i.e., $Z_{\text{Drug}} \leq 2.4$ (Figure 1D). In this category (Figure S2C), the effect of gene loss in the presence of drug is eliminated or milder relative to what is observed in the presence of DMSO (and thus there is enrichment in drug versus DMSO, which qualifies the gene for a buffering interaction). We describe these interactions as epistatic buffering, a term used in genetics to describe the non-additive effects of two deleterious gene disruptions. Not surprisingly, many of these epistatic buffering interactions are intra-mitochondrial (Figures S2B and S2C). We subsequently validated the buffering interaction between REXO2 loss and ethidium bromide in individually targeted CRISPR KO cells (Figure S4B), providing confirmation to a previous report that REXO2 loss can be tolerated by mammalian rho⁰ cells lacking mtDNA (Bruni et al., 2013). REXO2 encodes a mitochondrial protein that appears to be involved in mitochondrial nucleic acid degradation. Genes involved in mitochondrial RNA processing are generally buffered under ethidium bromide (Figure S4C). The processes downstream of mtDNA, such as mtRNA processing, are presumably no longer operative in the absence of mtDNA.

We identified a novel extra-mitochondrial epistatic buffering interaction between the loss of LARP1, which encodes a cytosolic protein, and oligomycin (Figure 5A). LARP1 loss also exhibits a sub-threshold interaction with ethidium bromide (Figure 5A). The buffering of LARP1 loss by mitochondrial inhibitors raises the hypothesis that LARP1 is involved in OXPHOS biology. Indeed, knocking out LARP1 gene in K562 leads to a partial reduction in oxygen consumption under basal and maximal respiration (Figure 5B). We also performed the glucose/galactose death assay as described in Arroyo et al. (2016) and showed that LARP1 loss leads to increased cell death in galactose but not in glucose (Figure 5C). Both results suggest that LARP1 is required for intact OXPHOS capacity.

LARP1 is known to regulate cytosolic translation through binding to mRNA containing the 5' terminal oligopyrimidine (TOP) motif, in response to mammalian target of rapamycin (mTOR) signaling (Fonseca et al., 2015; Tcherkezian et al., 2014). While LARP1 homologs in *S. cerevisiae* (Kershaw et al., 2015) and *Drosophila* (Zhang et al., 2016) have been shown to regulate mitochondrial protein abundance, to our knowledge, involvement of LARP1 in the regulation of OXPHOS has not been previously reported in human or mammalian systems. To predict the specific function of LARP1 with human mitochondria, we considered co-dependency profiles (Figure 5D) across our chemical-

genetic compendium to predict gene function (see STAR Methods). Co-dependency profiling reveals LARP1 to be one of the few non-mitochondrial proteins within a tight cluster that is functionally related to mitochondrial translation (Figure S4A). Consistent with the hypothesis of LARP1 being involved in mitochondrial translation, the abundance of mtDNA-encoded MT-CO1 and MT-CO2 is reduced in LARP1 KO (Figure 5E). This reduction in MT-CO1 and MT-CO2 upon LARP1 loss without an apparent effect on mtDNA copy number (Figure 5F) or mtRNA level (Figure 5G) is consistent with a role in mitochondrial translation for LARP1. LARP1 loss also affects a subset of nuclear encoded mitochondrial proteins, notably complex I (NDUFB8) and complex II (SDHB) subunits (Figure 5E). The mechanism by which oligomycin or ethidium bromide, but not other mitochondrial inhibitors, buffers the loss of genes involved in mitochondrial translation including LARP1 (Figures S4A and S4D), requires further investigation.

Genes Whose Loss Suppresses the Toxic Effects of Mitochondrial Inhibitors

Among the collection of genes broadly characterized as buffering, we report 63 suppressors whose loss alleviates the toxic growth effects of mitochondrial inhibitors (Figure 2B). Our screening data predict that knocking out these genes can genuinely reduce or reverse the proliferative defects of mitochondrial dysfunction. The losses of these genes either play an active role in compensating for or protecting against the underlying pathophysiology, or they prevent drug toxicity. This group of chemical-genetic interactions includes two recently identified genetic suppressors of mitochondrial dysfunction, *ATPIF1* and *vHL*, while providing new information into the specificity of their suppressive actions. We find that loss of *ATPIF1* suppresses the growth effects of antimycin+oligomycin and ethidium bromide but does not effectively suppress toxicity from piericidin, metformin, antimycin, oligomycin, or chloramphenicol (Figure 2B). This pattern is consistent with the notion that *ATPIF1* is a strong genetic suppressor under drug treatments that compromise mitochondrial membrane potential (Chen et al., 2014). Co-treatment with antimycin+oligomycin collapses membrane potential acutely, whereas ethidium bromide depletes membrane potential more slowly due to chronic loss of both the electron transport chain and complex V. As *ATPIF1* functions as an inhibitor of the ATPase activity of complex V, loss of *ATPIF1* allows reversal of complex V to defend the membrane potential. This result points to the essential role of membrane potential for cell survival under severe mitochondrial dysfunction, consistent with classic results in *S. cerevisiae* (Veatch et al., 2009).

Loss of *vHL*, in contrast, suppresses antimycin, oligomycin, and antimycin+oligomycin but does not suppress other drugs including ethidium bromide. Of note, our screen has also identified *TCEB2*, which co-expresses with OXPHOS transcripts (Baughman et al., 2009) while its gene product physically interacts with vHL protein (Stebbins et al., 1999). Our screen has also revealed numerous genetic suppressors not previously reported—notably complex I genes (which we discuss later) and nuclear factors such as *NAIF1*, *NR2F2*, and *SIN3A* and its corepressor complex component *SUDS3*, *KLF16*, *C7orf26*, and the PP2A regulator *FAM122A* (Figure 2B).

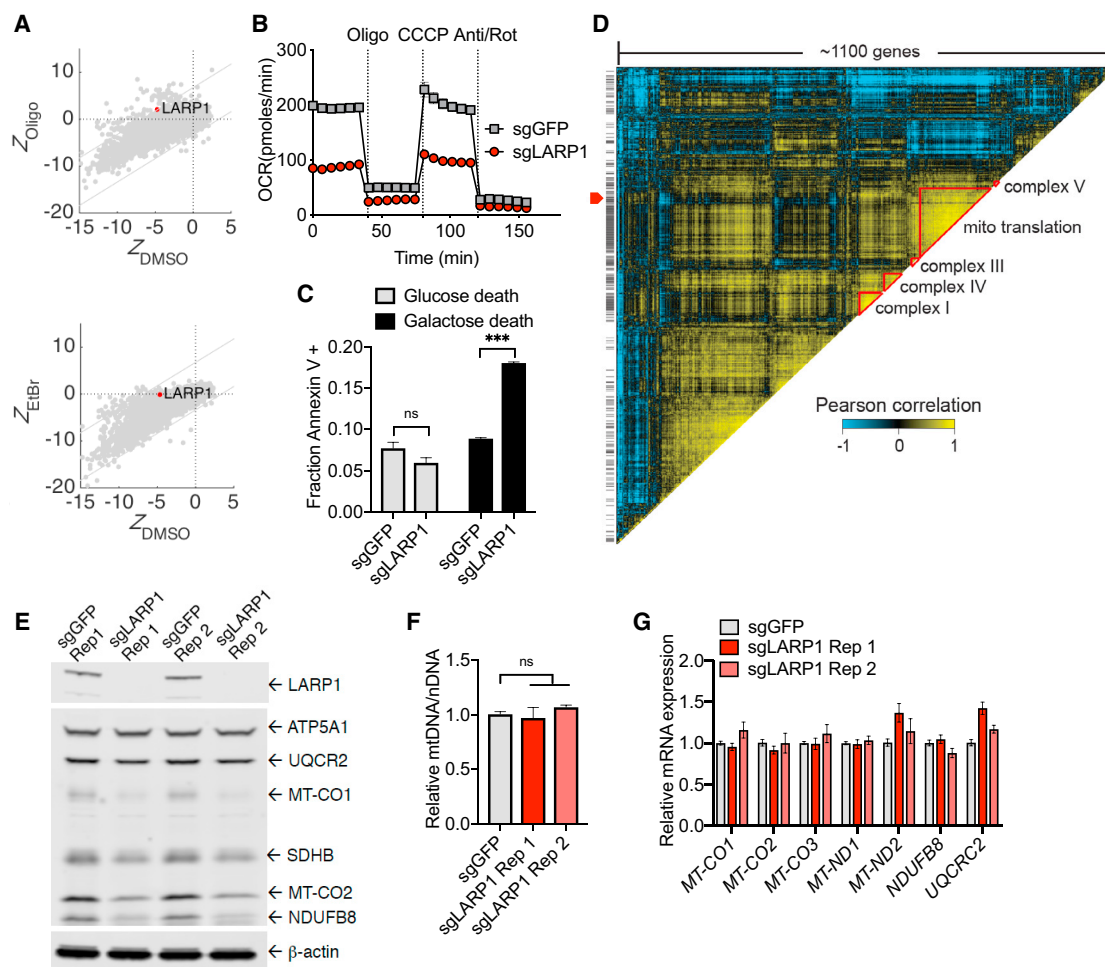


Figure 5. Loss of Cytosolic Protein LARP1 Is Buffered under OXPHOS Inhibition

(A) Scatterplots of Z scores highlighting KO of LARP1 in oligomycin (top) or ethidium bromide (bottom) versus DMSO. The gray dotted lines represent the cutoffs for interactions.

(B) Oxygen consumption as assessed by the Seahorse Extracellular Flux (XF96) Analyzer in K562 cells with sgRNAs directed against the genes indicated (average \pm SEM, $n = 6$).

(C) Cell death as assessed by Annexin V staining and flow cytometry in K562 cells cultured in glucose or galactose containing medium with sgRNAs directed against the genes indicated (average \pm SEM, $n = 3$).

(D) Heatmap of co-dependency based on hierarchical clustering of Pearson correlations between the mean log₂-fold changes across sgRNAs for genes. Disjoint modules (demarcated with red triangles) were annotated by assigned Gene Ontology (GO) term that was significantly enriched in that cluster (hypergeometric $p \leq 10^{-10}$). Black ticks represent genes that are listed in the MitoCarta2.0 database (Calvo et al., 2016). The red arrow denotes LARP1.

(E) Immunoblots for the specified mitochondrial proteins and LARP1 in K562 cells with sgRNAs directed against the genes indicated. A representative experiment is shown.

(F) Real-time PCR-based measurement of mtDNA relative to nuclear DNA (nDNA) in K562 cells with sgRNAs directed against the genes indicated (average \pm SEM, $n = 3$).

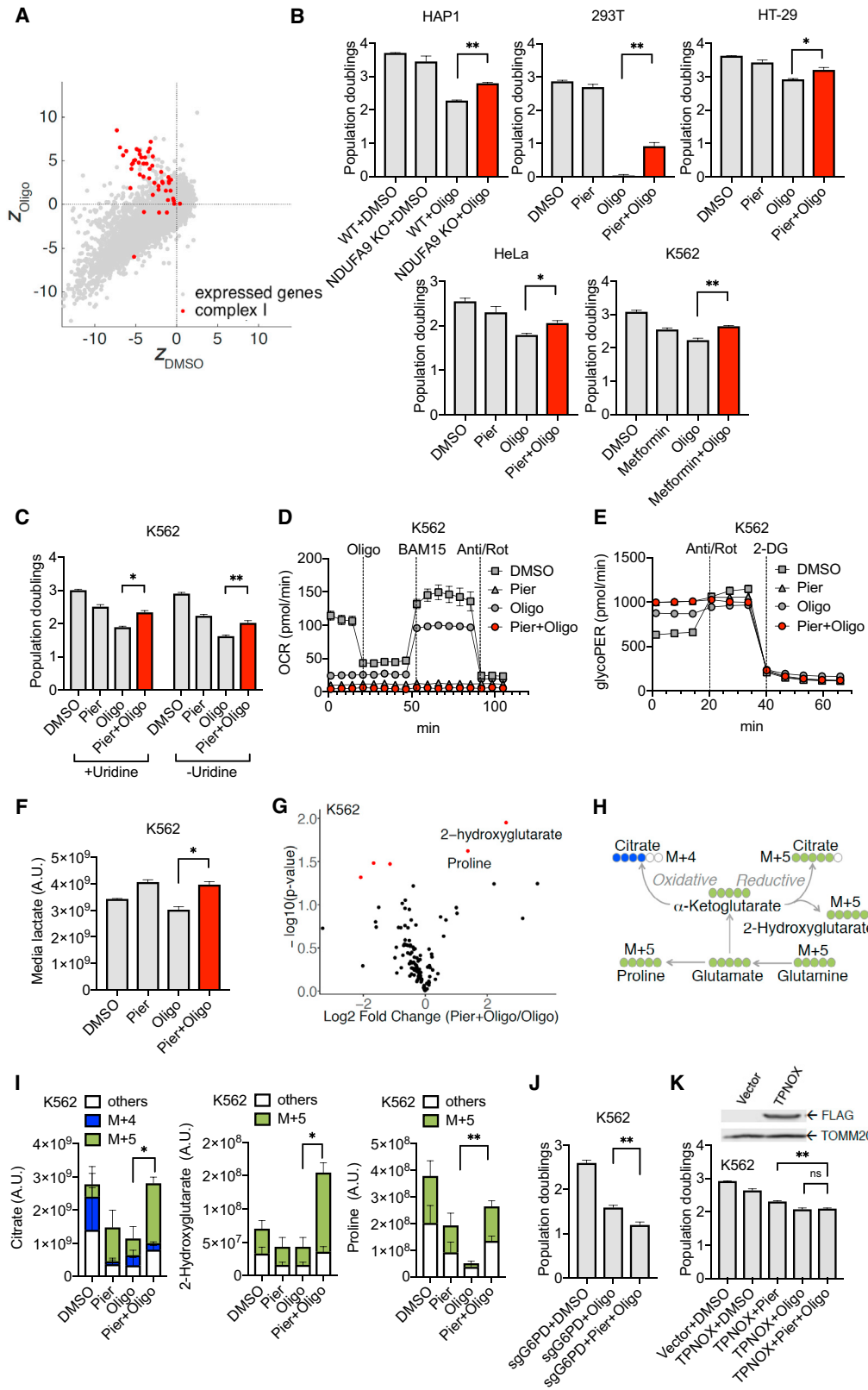
(G) Taqman gene expression analysis of transcripts of OXPHOS components in K562 cells with sgRNAs directed against the genes indicated (average \pm SEM, $n = 3$). For (C) and (F), ns $p > 0.05$ or *** < 0.001 indicates two-tailed Student's t test p value.

See also Figure S4.

Suppression of Oligomycin's Toxicity by Simultaneous Loss of Mitochondrial Complex I

Our screen has also identified numerous genetic suppressors not previously reported, but perhaps most striking, we find that many complex I subunits appear to score as genetic suppressors of oligomycin. Complex I represents the entry point to the electron transport chain and consists of ~ 45 subunits, 38 of

which are encoded by the nuclear genome. KOs of a very large number of nuclear-encoded subunits and assembly factors are enriched under oligomycin (Figure 6A) and, to a lesser extent, antimycin+oligomycin (Figure S5A). Enrichment of complex I KOs is weaker with antimycin treatment and is not observed with other drug treatments (Figure S5A). We validated the alleviation of oligomycin's toxicity by *NDUFA9* loss (Figure 6B) and



(legend on next page)

confirmed its drug specificity as only epistatic buffering effects were observed under piericidin or antimycin (Figure S5B). In addition, we found that the specific complex I inhibitor piericidin can alleviate oligomycin's toxicity in multiple cell lines (Figure 6B). Metformin, which targets complex I, can also alleviate oligomycin's toxicity (Figure 6B).

While the loss of complex I can robustly alleviate oligomycin's toxicity, the converse is not true as the loss of complex V components, with the possible exception of ATP5A1, is not alleviated or buffered by chemical inhibitors of complex I. The lack of reciprocity of interaction is likely due to the non-equivalence of pharmacologic inhibition of complex V and biallelic genetic loss of a component of complex V. Under oligomycin treatment, complex V is intact and OXPHOS is inhibited, typically leading to mitochondrial membrane hyperpolarization. On the other hand, biallelic genetic loss of a complex V subunit may lead to a different outcome since complex V can defend membrane potential through reversal of activity, as well as dissipate it. Moreover, the F1-ATPase of complex V has been implicated in the maintenance of mtDNA (Contamine and Picard, 2000). As such, biallelic loss of a complex V component may affect the stability of other complexes of the electron transport chain or impact their expression due to defective mtDNA maintenance, which is not recapitulated by oligomycin action. Therefore, while the intra-OXPHOS suppression of complex V dysfunction by complex I loss has not been previously reported to our knowledge, it is restricted to specific modes of complex V inhibition modeled by oligomycin.

Suppression of Oligomycin's Toxicity by Complex I Loss Is Not Simply Explained by Deficiency of Pyrimidines or Toxicity of Reactive Oxygen Species

We first sought to determine whether an important resource required for proliferation is depleted under oligomycin but

restored when complex I activity is simultaneously inhibited. One candidate is pyrimidines, as it has been shown that OXPHOS dysfunction leads to a stalling of dihydroorotate dehydrogenase (DHODH), a rate-limiting enzyme in *de novo* pyrimidine biosynthesis that requires oxidized coenzyme Q as a cofactor (Khutomenko et al., 2010). Though not well appreciated, complex I inhibition can actually upregulate *de novo* pyrimidine biosynthesis (Shaham et al., 2010), owing to the fact that complex I inhibition makes a larger part of the oxidized Q pool available for other Q-linked enzymes including DHODH. Such a mechanism may be especially important when reoxidation of the coenzyme Q pool is limited or disabled with a blockade downstream (e.g., antimycin or oligomycin treatment). However, pyrimidine deficiency cannot explain the suppression by complex I inhibition, as uridine was supplemented during screening and validation (Figures 6B and 6C). In addition, the interaction between complex I and complex V occurs to a similar extent when uridine is not supplemented and dialyzed serum is used (Figure 6C). In K562 cells, the uridine salvage pathway is operative as evidenced by the fact that loss of uridine-cytidine kinase UCK2 is synthetic lethal with antimycin (Figure 2A), a condition under which reoxidation of coenzyme Q is blocked and *de novo* pyrimidine synthesis is disabled, causing the cells to rely entirely on uridine salvage for pyrimidines. As such, pyrimidine levels are presumably supported by the salvage pathway, arguing against restoring *de novo* pyrimidine synthesis as the key mechanism of suppression.

We next sought to determine whether oligomycin leads to the buildup of a toxin that can be cleared when complex I is simultaneously inhibited, the most obvious candidate being some form of reactive oxygen species (ROS). Oligomycin treatment hyperpolarizes the mitochondrial membrane potential (as it prevents the proton gradient from being dissipated for ATP synthesis) and is a known driver of ROS formation, either by

Figure 6. Suppression of Oligomycin's Toxicity by Loss of Complex I Activity

(A) Scatterplot of the fitness of a gene KO in oligomycin (Z_{Oligo}) versus its fitness in DMSO (Z_{DMSO}). Gray dots denote all 11,102 genes in the analysis, and the red dots denote 50 nuclear genes that encode structural subunits and assembly factors of complex I.

(B) Validation of *NDUFA9* loss, piericidin, and metformin as suppressors of oligomycin in HAP1, 293T, HT-29, HeLa, and K562 cells. Cell counts were performed 3 days post drug treatment (average \pm SEM, $n = 3$).

(C) Validation of piericidin as a suppressor of oligomycin in K562 in the presence (+Uridine) or absence (–Uridine) of 50 $\mu\text{g}/\text{mL}$ uridine supplementation. Dialyzed serum was used for –Uridine growth. Cell counts were performed 3 days post drug treatment (average \pm SEM, $n = 3$). In (B) and (C), * $p < 0.05$ or ** $p < 0.01$ indicates two-tailed Student's *t* test *p* value.

(D) Oxygen consumption as assessed by the Seahorse Extracellular Flux (XF96) Analyzer in K562 cells after 3 days of drug treatment (average \pm SEM, $n = 12$).

(E) Corrected extracellular acidification rate as assessed by the Seahorse Extracellular Flux (XF96) Analyzer in K562 after 3 days of drug treatment (average \pm SEM, $n = 12$).

(F) Media lactate levels in K562 using targeted mass spectrometry after 3 days of drug treatment (average \pm SEM, $n = 3$). * $p < 0.05$ indicates two-tailed Student's *t* test *p* value.

(G) Volcano plot comparing piericidin+oligomycin to oligomycin from full-scan metabolomics in K562 using mass spectrometry after 3 days of drug treatment (average of $n = 3$). Highlighting in red indicates * $p < 0.05$ two-tailed Student's *t* test *p* value.

(H) Schematics for stable isotope labeling with [$U\text{-}^{13}\text{C}$]glutamine to monitor ^{13}C incorporation in key metabolites.

(I) Total metabolite pools and ^{13}C labeling pattern of citrate, 2-hydroxyglutarate, and proline over the course of 8 h upon tracer analysis with [$U\text{-}^{13}\text{C}$]glutamine in K562 cells. Cells were pretreated in uridine-free medium 48 h prior to [$U\text{-}^{13}\text{C}$]glutamine supplementation (average \pm SEM, $n = 3$). * $p < 0.05$ or ** $p < 0.01$ indicates two-tailed Student's *t* test *p* value.

(J) Growth phenotypes of K562 cells with sgRNAs directed against *G6PD* under oligomycin or piericidin+oligomycin treatment. Cell counts were performed 3 days post drug treatment (average \pm SEM, $n = 3$). ** $p < 0.01$ indicates two-tailed Student's *t* test *p* value.

(K) Growth phenotypes of cells stably expressing a vector vehicle or cytosolic TPNOX under the specified treatment in K562. Cell counts were performed 3 days post drug treatment (average \pm SEM, $n = 3$). ns $p > 0.05$ or ** $p < 0.01$ indicates two-tailed Student's *t* test *p* value. Top shows immunoblots for FLAG and the TOMM20 loading control for cells expressing either the vector vehicle or cytosolic TPNOX.

See also Figure S5.

succinate-driven reverse electron transport (RET) (Chouchani et al., 2014) or via over-reduced states of the CoQ and NADH pools (Robb et al., 2018). We confirmed that oligomycin hyperpolarizes mitochondria in K562, and such hyperpolarization can be suppressed by simultaneous treatment with piericidin or the mitochondria-specific uncoupler BAM15 (Kenwood et al., 2014) (Figure S5C). Simultaneous administration of an intermediate dose (1 μ M) of uncoupler improves proliferation under oligomycin (Figure S5D). However, the level of oligomycin-induced mitochondrial superoxide is suppressed by BAM15 only when a high concentration (5 mM) of succinate is provided, but not under normal culture condition (Figure S5E). Piericidin significantly increases mitochondrial superoxide under oligomycin (Figure S5E) in K562, which does not support complex I-RET being a significant source of mitochondrial superoxide. Furthermore, administration of antioxidants, including the specific complex I-RET inhibitor S1QEL (Brand et al., 2016), does not suppress oligomycin's toxicity (Figure S5F). Hence, oligomycin's toxicity, and the mechanism by which it is suppressed by complex I loss, cannot be simply explained by ROS toxicity.

Inhibiting Complex I Activity Rebalances Redox Cofactors and Promotes Glycolysis and Reductive Carboxylation under Oligomycin Treatment

Next, we investigated the bioenergetic and metabolic consequences of complex I inhibition on oligomycin-treated cells. As measured using a Seahorse XFe96 Extracellular Flux Analyzer (Agilent), inhibition of complex I with piericidin eliminates oligomycin-resistant respiration (Figure 6D), arguing against a suppression mechanism that involves reactivation of electron transport chain activity such as the alleviation enabled by uncouplers. When OXPHOS is dysfunctional, glycolysis is capable of compensating for ATP production as long as glucose is provided in the culture medium. As ATP availability is crucial for proliferation, we next asked whether elevated glycolysis is part of the suppression mechanism by complex I loss. We measured glycolytic rates with a Seahorse assay termed GlycoPER (see STAR Methods) and found it to be higher under piericidin+oligomycin than oligomycin alone in multiple cell lines (Figures 6E and S5G). To buttress the Seahorse results, we measured media lactate levels in K562 using targeted mass spectrometry and observed an elevated lactate excretion under piericidin+oligomycin (Figure 6F). Furthermore, we found that pyruvate supplementation is essential for complex I inhibition to alleviate oligomycin's toxicity (Figure S5H), as pyruvate withdrawal renders piericidin treatment detrimental to oligomycin-treated cells. Under OXPHOS inhibition, pyruvate supplementation is required for NADH oxidation by the cytosolic lactate dehydrogenase to regenerate NAD^+ for glycolysis (King and Attardi, 1989; Titov et al., 2016), consistent with glycolysis being instrumental for the alleviation.

To more broadly characterize the metabolic changes that arise from a combined piericidin+oligomycin treatment, we performed full-scan intracellular metabolomics using mass spectrometry in K562 cells. We identified 2-hydroxyglutarate (2-HG) to be the most upregulated, statistically significant metabolite under piericidin+oligomycin when compared to oligomycin

alone, followed by the non-essential amino acid proline, which is not in the media used (Figure 6G). The elevation of 2-HG has been linked to reductive carboxylation of α -ketoglutarate (Mullen et al., 2014), presumably as a consequence of a higher NADH/NAD^+ ratio under mitochondrial dysfunction or hypoxia (Mullen et al., 2011; Wise et al., 2011). The whole cell NADH/NAD^+ ratio is substantially elevated under piericidin+oligomycin (Figure S5I) when compared to oligomycin alone in our system, with a redox cofactor balance that favors reductive synthesis.

To confirm that reductive carboxylation is indeed promoted under combined piericidin+oligomycin treatment, we cultured K562 cells under DMSO, oligomycin, or piericidin+oligomycin with [^{13}C]glutamine and monitored ^{13}C incorporation in tricarboxylic acid (TCA) cycle intermediates and other key metabolites over the course of 8 h using mass spectrometry. Oxidative metabolism of uniformly labeled ^{13}C -glutamine generates M+4 citrate, whereas reductive biosynthesis leads to M+5 citrate (Figure 6H). Glutamine-derived proline and 2-HG also contain five glutamine-derived ^{13}C (M+5). Indeed, reductive synthesis of citrate from glutamine, as identified by the level of M+5 citrate, significantly increases under piericidin+oligomycin when compared to oligomycin alone (Figure 6I). While oligomycin reduces the overall citrate level, piericidin+oligomycin restores the citrate to a level comparable to the DMSO control. We observed an increased reliance on reductive synthesis of citrate under piericidin+oligomycin across multiple cell lines (Figure S5J). We also observed a significant increase in 2-HG under piericidin+oligomycin. The 2-HG is produced primarily from glutamine as indicated by the M+5 mass isotopomer (Figure 6I), providing additional evidence for an elevated flux in reductive carboxylation of α -ketoglutarate by one of the NAD(P)H -dependent dehydrogenases. Finally, the intracellular proline pool, whose level is restored under piericidin+oligomycin, contains a significant fraction derived from glutamine as evidenced by M+5 mass isotopomer, likely because proline can be derived from glutamate in an NADH - and NADPH -dependent pathway (Phang et al., 2015). An increase in proline from glutamine source implicates an intracellular redox state that favors reductive biosynthesis, consistent with the observed elevation of 2-HG and M+5 citrate.

Since reductive biosynthesis is largely driven by the reducing power of cytosolic NADPH , we sought to determine whether the ability to suppress oligomycin by complex I inhibition is sensitive to the availability of cytosolic NADPH . First, we used *G6PD* KO, whose loss is synthetic lethal with complex I inhibition (Figure 3B), to reduce the formation of cytosolic NADPH and observed a more severe proliferation defect under piericidin+oligomycin than oligomycin alone (Figure 6J). Next, we expressed the genetically encoded, water-forming NADPH oxidase TPNOX (Cracan et al., 2017) to promote consumption of cytosolic NADPH and found that it blunted the suppression of oligomycin's toxicity by complex I inhibition (Figure 6K). Both results support the involvement of reductive carboxylation in the suppression by complex I loss, as cytosolic NADPH is heavily used in reductive biosynthesis within cells (e.g., citrate, fatty acids, and proline). Collectively, these experiments demonstrate that, in the setting of complex V inhibition, simultaneous

loss of complex I boosts fitness via a mechanism that involves promoting glycolysis and reductive carboxylation through rebalancing redox cofactors.

DISCUSSION

We have utilized a CRISPR screening approach to discover new genetic modifiers of mitochondrial dysfunction. In total, we report chemical-genetic interactions involving 191 genes, of which 38 are classified as synthetic sick/lethal, 63 are suppressors, and 91 are epistatically buffering (one gene is classified in two categories). Our compendium recovers recently reported genetic suppressors (*ATPIF1* and *vHL*), as well as genes involved in synthetic sick/lethal interactions (*GOT1*) and epistatic buffering (*REXO2*). We have been able to validate multiple novel interactors, namely *G6PD*, *PFKP*, *GPX4*, *LARP1*, and complex I. We have illustrated the utility of this compendium via four vignettes that explore some of the strongest hits identified.

More than half of the 101 genes that are suppressors or synthetic sick/lethal hits (Figure 2) participate in only one chemical-genetic interaction, consistent with the notion that mitochondrial lesions each have very distinct patterns of genetic interactions. Our work provides unexpected genetic insights into the connectivity of OXPHOS both within mitochondria and with the rest of the cell. While 35% of the synthetic sick/lethal or candidate suppressor genes we report encode proteins resident outside of mitochondria (underscoring the coupling between processes within the organelle and the remainder of the cell), we were surprised to find that 65% of these genetic modifiers involve genes encoding mitochondrial proteins, far greater than expected by chance given that only 6% of all nuclear genes encode mitochondrial proteins. This observation reflects the fact that many pathways within the organelle locally sense and modify mitochondrial lesions. The enrichment of intra-organelle genetic interactions relative to inter-organelle interactions has been observed in previously reported yeast genetic interaction screens (Cossanzo et al., 2016; Hoppins et al., 2011). To the best of our knowledge, the extent of intra-organelle interactions in mammalian biology is underappreciated and has not been previously reported. In the coming years, as chemical-genetic and related approaches are applied to other organelles, it will be interesting to see whether a similar pattern of intra-organelle versus extra-organelle interactions emerges in mammalian systems.

Extra-mitochondrial synthetic sick/lethal interactions are exemplified by genes involved in glycolysis or the pentose phosphate pathway. Genes associated with glycolysis are expected to be indispensable under OXPHOS inhibition, as glycolytic ATP production becomes essential in the face of OXPHOS dysfunction. The phosphofructokinase 1 (PFK-1), for which *PFKP* encodes one of its three isozymes, represents a key step that commits glucose to glycolysis and is tightly regulated by multiple metabolites (Mor et al., 2011). *PFKP* has been shown to be highly upregulated by Ras oncogene (Tanner et al., 2018) and stabilized by AKT in glioblastoma (Lee et al., 2017) and is implicated in promoting aerobic

glycolysis. A highly regulated component of glycolysis, *PFKP* may play an especially important role in determining the utilization and fate of glucose when OXPHOS is inhibited. The pentose phosphate pathway gene *G6PD* is particularly important for NADPH homeostasis as it encodes the enzyme that generates the vast majority of cytosolic NADPH (Chen et al., 2019). Cytosolic NADPH production might become increasingly important in the face of OXPHOS dysfunction, as it is implicated in the reductive biosynthesis of citrate and fatty acids and important in ROS defense.

Our work suggests that the intra-mitochondrial synthetic sick/lethal hit *GPX4* may be a part of a homeostatic feedback loop designed to guard against mitochondrial dysfunction. The upregulation of *GPX4* in response to OXPHOS dysfunction could be controlled by a nuclear transcriptional program, such as the ATF4-dependent integrated stress response (Bao et al., 2016). It is notable that *GPX4* is also normally induced during the PGC-1 α transcriptional program for mitochondrial biogenesis (Mootha et al., 2004), indicating that this is likely part of a physiologic relationship whereby elevated OXPHOS activity is met with an increased need for *GPX4*. The interaction between OXPHOS dysfunction and loss of *GPX4* is richly supported by *in vivo* reports of patients with mitochondrial disease, who can show elevated levels of toxic byproducts of lipid hydroperoxides such as malondialdehyde and 4-hydroxynonenal (Thompson Legault et al., 2015), and combined with the current screening results, raise the question of whether lipid peroxidation contributes to mitochondrial pathogenesis. OXPHOS dysfunction may lead to altered glutathione and NADPH metabolism, both of which play very important roles in the prevention of lipid peroxidation and *GPX4* activity. Disrupting glutathione metabolism using erastin or buthionine sulfoximine, or by cysteine starvation, has been shown to induce ferroptotic cell death (Dixon et al., 2012; Gao et al., 2019). As previously discussed, our screens reveal that loss of *G6PD* exacerbates the growth defect caused by OXPHOS inhibition, raising the question of whether this interaction can be related to ferroptosis, as the pentose phosphate pathway is a major source of cellular NADPH for reductive synthesis of fatty acids and lipids. Lipid metabolism represents another important aspect for the regulation of ferroptosis (Doll et al., 2017; Zou et al., 2019). It was recently reported that inhibition of complexes I–IV of the electron transport chain suppresses ferroptosis induced by cysteine deprivation, specifically in cell lines that do not tolerate *GPX4* loss (Gao et al., 2019). In contrast, our work suggests that the expression of *GPX4* is induced in response to OXPHOS dysfunction and that the inhibition of ATP synthase by oligomycin sensitizes cells to ferroptotic death when *GPX4* is also inhibited. Future studies will be required to reconcile these related findings and how they operate *in vivo* in states such as cancer.

We find that loss of the cytosolic protein *LARP1* is itself toxic, but it's less toxic than expected in the setting of OXPHOS inhibition. Such a buffering interaction raises the hypothesis that *LARP1* is functionally related to OXPHOS, which we experimentally confirm. Co-dependency profiles predict cytosolic *LARP1* to regulate intra-mitochondrial protein translation, which we

support with experimental evidence. While our finding represents the first report linking human LARP1 to mitochondrial function, previous studies have shown that LARP1 homologs in *S. cerevisiae* can affect the expression of many nuclear-encoded mitochondrial proteins (Kershaw et al., 2015). Likewise, a previous paper (Zhang et al., 2016) showed that the *Drosophila* homolog of LARP1 is recruited to the outer mitochondrial membrane and is involved in the synthesis of nuclear-encoded mitochondrial proteins. As both human LARP1 and mTOR signaling have been shown to regulate translation through the 5' TOP motifs (Fonseca et al., 2015; Thoreen et al., 2012), it will be interesting to determine whether TOP motifs are harbored at the 5' UTR of any nuclear encoded genes that are important for mitochondrial translation and whether mTOR is capable of regulating their expression.

One of the most surprising and striking intra-mitochondrial genetic suppressors we have identified is the alleviation of complex V dysfunction by simultaneous loss of complex I. Such an intra-mitochondrial interaction could not have been discovered by genetic interaction mapping in *S. cerevisiae*, as *S. cerevisiae* does not have a macromolecular complex I. We note that this type of intra-system suppression has previously been described in the context of antibiotic actions (Bollenbach et al., 2009; Yeh et al., 2009), but to our knowledge, it has never before been reported in a mammalian system, and certainly not described in the context of mitochondrial physiology. A very large number of distinct genetic losses of complex I subunits suppress the toxicity of oligomycin (Figure 6A). We validate that *NDUFA9* loss, piericidin, or metformin can eliminate the toxic effect of oligomycin (Figures 6B and 6C).

The validation of complex I as a true suppressor of OXPHOS dysfunction may help explain key observations from disease biology. Our work implies fitness benefits of complex I loss under certain circumstances, raising the question of whether it contributes to the proliferation of certain types of cancers such as renal oncocytoma and Hurthle cell thyroid carcinoma, in which complex I loss is shown to be a driver event (Gopal et al., 2018a, 2018b). It will be interesting to test whether certain aspects of oligomycin's effects, such as oligomycin-resistant respiration, mitochondrial hyperpolarization, or susceptibility to lipid peroxidation, are prominent in the cells of origin of these cancers such that loss of complex I is favorable. Moreover, our genetic interactions also support the notion that metformin targets complex I, and the unanticipated interaction between complex I and oligomycin raises a new mechanistic hypothesis about how metformin may alleviate aging (Barzilai et al., 2016). Specifically, the widely documented age-associated decline in mitochondrial OXPHOS activity (Trounce et al., 1989) may have cellular pathologies that are actually alleviated by inhibition of complex I via drugs such as metformin. Notably, it has been shown in *C. elegans* that a significant decline in ATP-linked oxygen consumption occurs over aging (Huang and Lin, 2018), implicating the loss of complex V activity as a signature for worm aging. Our work raises the specific hypothesis that metformin's ability to prolong lifespan at the organismal level may be related to its ability to suppress complex V inhibition at the cellular level. The ability of complex I loss to improve

fitness of OXPHOS-limited cells could be related to the organismal loss of complex I subunits, which have occurred at least four times in eukaryotic evolution (Pagliarini et al., 2008).

Mechanistically, we show that loss of complex I activity increases glycolysis, promotes reductive carboxylation, and prevents mitochondrial hyperpolarization, all of which benefit cells under complex V inhibition. Our results are consistent with the observation that glycolysis and reductive carboxylation are mechanistically connected via NADH and NADPH redox cofactors (Brodsky et al., 2019; Gaude et al., 2018). Moreover, reductive synthesis of biomolecules such as citrate and proline may act as a "sink" for excessive reducing equivalents. Such rebalancing of redox networks may improve cell proliferation by optimizing electron flow while providing building blocks such as nucleotides, amino acids, and lipids. In *E. coli*, mutations that rebalance redox cofactors can result in metabolic flexibility and improved fitness (Long et al., 2018). Perhaps in mammalian systems, such "malleability" in metabolic networks is exploited by elimination of complex I activity when complex V is inhibited with oligomycin.

We anticipate that our inventory of chemical-genetic interactions can be useful in many ways for the biomedical research community. First, it helps to nominate new drug targets that are capable of specifically suppressing different types of mitochondrial dysfunction. An entire collection of such targets is valuable given the growing types of mitochondrial dysfunction that are linked to rare and age-associated common human diseases. Perhaps counterintuitively, our work suggests that one way to suppress mitochondrial dysfunction is to actually inhibit a "second site" within mitochondria. Second, our inventory may help to nominate new drug combinations where monotherapy leads to a mitochondrial vulnerability that could also be targeted pharmacologically, as in certain cancers. Third, it will help to identify either inherited genetic factors or perhaps tissue-specific programs that may help explain the penetrance and tissue specificity of mitochondrial disease. For example, our work raises the specific hypothesis that G6PD deficiency, which is found in hundreds of millions of individuals, may serve as a novel genetic modifier of mitochondrial disease. Finally, our work may have very basic implications for understanding mitochondrial evolution. Over millions of years of evolution, mitochondria have been effectively hard-wired within our cells—with nearly all of the original endosymbiont's genes either completely lost or transferred to the nuclear genome, with brand new functionality encoded in the nuclear genome (Vafai and Mootha, 2012). The rich set of genetic interactions we've identified will help us to decipher the full regulatory and metabolic logic of this ancient compartmentalization.

STAR★METHODS

Detailed methods are provided in the online version of this paper and include the following:

- KEY RESOURCES TABLE
- LEAD CONTACT AND MATERIALS AVAILABILITY

- **EXPERIMENTAL MODEL AND SUBJECT DETAILS**
 - Cell Lines
- **METHOD DETAILS**
 - Determination of Infection Conditions for CRISPR Pooled Screens
 - Genome Scale CRISPR Screens with Brunello All-in-one Library
 - Gene-Specific CRISPR-Cas9 Knockouts
 - Gene-Specific cDNA Rescue
 - TPNOX Expression
 - Cell Death Assay
 - Oxygen Consumption by the Seahorse XF Analyzer
 - Glycolytic Rate Assay by the Seahorse XF Analyzer
 - Polyacrylamide Gel Electrophoresis and Protein Immunoblotting
 - Quantification of mtDNA by Real-Time PCR
 - Mitochondrial Membrane Potential Measurement
 - Growth Experiments
 - Lipid Peroxidation Measurement
 - Mitochondrial Superoxide Measurement
 - Isolation of Mitochondria
 - Immunofluorescence Experiment
 - Gene Expression Assay by Real-Time PCR
 - Intracellular Metabolite Profiling using Liquid Chromatography-Mass Spectrometry (LCMS):
 - NADH/NAD⁺ Analysis using LCMS
 - Stable Isotope Analysis of [U-¹³C]glutamine
 - Media Lactate Analysis
- **QUANTIFICATION AND STATISTICAL ANALYSIS**
 - Gene Scoring
 - Pathway Analysis
 - Hierarchical Clustering
- **DATA AND CODE AVAILABILITY**

SUPPLEMENTAL INFORMATION

Supplemental Information can be found online at <https://doi.org/10.1016/j.cell.2019.10.032>.

ACKNOWLEDGMENTS

We thank Dan Gottschling, David Botstein, Calvin Jan, Vasanthi Viswanathan, Sarah Calvo, and Jordan Wengrod for their valuable feedback on the manuscript and Jason Arroyo, Matthew Broadus, and Lev Sandler for technical assistance. This work was supported by funding from Calico Life Sciences (S.B.V.) and NIH R35GM122455 (V.K.M.). V.K.M. is an investigator of the Howard Hughes Medical Institute.

AUTHOR CONTRIBUTIONS

Conceptualization, T.-L.T., S.B.V., and V.K.M.; Investigation, T.-L.T., A.M.C., H.S., W.H.W.H., Y.L., S.H.K., D.H.F.R., R.H.B., S.R., F.P., A.G., and Z.K.; Resources, J.K.E., S.L.S., and J.G.D.; Writing, T.-L.T., S.B.V., and V.K.M. with input from all authors; Supervision, V.K.M., S.B.V., and D.E.R.

DECLARATION OF INTERESTS

V.K.M. is a paid advisor to Raze Therapeutics, Janssen Pharmaceuticals, and 5AM Ventures. S.B.V. is currently an employee of Sanofi Pharmaceuticals. T.-L.T., S.B.V., and V.K.M. are listed as inventors on a provisional patent application submitted by the Broad Institute on technology described in this paper.

Received: January 21, 2019
 Revised: September 12, 2019
 Accepted: October 23, 2019
 Published: November 14, 2019

REFERENCES

- Arroyo, J.D., Jourdain, A.A., Calvo, S.E., Ballarano, C.A., Doench, J.G., Root, D.E., and Mootha, V.K. (2016). A Genome-wide CRISPR Death Screen Identifies Genes Essential for Oxidative Phosphorylation. *Cell Metab.* **24**, 875–885.
- Balaban, R.S., Kantor, H.L., Katz, L.A., and Briggs, R.W. (1986). Relation between work and phosphate metabolite in the in vivo paced mammalian heart. *Science* **232**, 1121–1123.
- Bao, X.R., Ong, S.E., Goldberger, O., Peng, J., Sharma, R., Thompson, D.A., Vafai, S.B., Cox, A.G., Marutani, E., Ichinose, F., et al. (2016). Mitochondrial dysfunction remodels one-carbon metabolism in human cells. *eLife* **5**, e10575.
- Barzilai, N., Crandall, J.P., Kritchevsky, S.B., and Espeland, M.A. (2016). Metformin as a Tool to Target Aging. *Cell Metab.* **23**, 1060–1065.
- Baughman, J.M., Nilsson, R., Gohil, V.M., Arlow, D.H., Gauhar, Z., and Mootha, V.K. (2009). A computational screen for regulators of oxidative phosphorylation implicates SLIRP in mitochondrial RNA homeostasis. *PLoS Genet.* **5**, e1000590.
- Benjamini, Y.H.Y. (1995). Controlling the False Discovery Rate: A Practical and Powerful Approach to Multiple Testing. *J. R. Stat. Soc. Series B.* **57**, 289–300.
- Birsoy, K., Wang, T., Chen, W.W., Freinkman, E., Abu-Remaileh, M., and Sabatini, D.M. (2015). An Essential Role of the Mitochondrial Electron Transport Chain in Cell Proliferation Is to Enable Aspartate Synthesis. *Cell* **162**, 540–551.
- Bollenbach, T., Quan, S., Chait, R., and Kishony, R. (2009). Nonoptimal microbial response to antibiotics underlies suppressive drug interactions. *Cell* **139**, 707–718.
- Brand, M.D., Goncalves, R.L., Orr, A.L., Vargas, L., Gerencser, A.A., Borch Jensen, M., Wang, Y.T., Melov, S., Turk, C.N., Matzen, J.T., et al. (2016). Suppressors of Superoxide-H₂O₂ Production at Site I_O of Mitochondrial Complex I Protect against Stem Cell Hyperplasia and Ischemia-Reperfusion Injury. *Cell Metab.* **24**, 582–592.
- Brodsky, A.N., Odenwelder, D.C., and Harcum, S.W. (2019). High extracellular lactate causes reductive carboxylation in breast tissue cell lines grown under normoxic conditions. *PLoS ONE* **14**, e0213419.
- Bruni, F., Gramegna, P., Oliveira, J.M., Lightowers, R.N., and Chrzanowska-Lightowlers, Z.M. (2013). REXO2 is an oligoribonuclease active in human mitochondria. *PLoS ONE* **8**, e64670.
- Calvo, S.E., Clauser, K.R., and Mootha, V.K. (2016). MitoCarta2.0: an updated inventory of mammalian mitochondrial proteins. *Nucleic Acids Res.* **44** (D1), D1251–D1257.
- Cappellini, M.D., and Fiorelli, G. (2008). Glucose-6-phosphate dehydrogenase deficiency. *Lancet* **371**, 64–74.
- Chance, B., and Williams, G.R. (1955). Respiratory enzymes in oxidative phosphorylation. I. Kinetics of oxygen utilization. *J. Biol. Chem.* **217**, 383–393.
- Chen, W.W., Birsoy, K., Mihaylova, M.M., Snitkin, H., Stasinski, I., Yucel, B., Bayraktar, E.C., Carette, J.E., Clish, C.B., Brummelkamp, T.R., et al. (2014). Inhibition of ATP1F1 ameliorates severe mitochondrial respiratory chain dysfunction in mammalian cells. *Cell Rep.* **7**, 27–34.
- Chen, L., Zhang, Z., Hoshino, A., Zheng, H.D., Morley, M., Arany, Z., and Rabinowitz, J.D. (2019). NADPH production by the oxidative pentose-phosphate pathway supports folate metabolism. *Nat. Metab.* **1**, 404–415.
- Chouchani, E.T., Pell, V.R., Gaude, E., Aksentijevic, D., Sundier, S.Y., Robb, E.L., Logan, A., Nadtochiy, S.M., Ord, E.N.J., Smith, A.C., et al. (2014). Ischaemic accumulation of succinate controls reperfusion injury through mitochondrial ROS. *Nature* **515**, 431–435.
- Cogliati, S., Frezza, C., Soriano, M.E., Varanita, T., Quintana-Cabrera, R., Corrado, M., Cipolat, S., Costa, V., Casarin, A., Gomes, L.C., et al. (2013). Mitochondrial cristae shape determines respiratory chain supercomplexes assembly and respiratory efficiency. *Cell* **155**, 160–171.

- Contamine, V., and Picard, M. (2000). Maintenance and integrity of the mitochondrial genome: a plethora of nuclear genes in the budding yeast. *Microbiol. Mol. Biol. Rev.* *64*, 281–315.
- Costanzo, M., VanderSluis, B., Koch, E.N., Baryshnikova, A., Pons, C., Tan, G., Wang, W., Usaj, M., Hanchard, J., Lee, S.D., et al. (2016). A global genetic interaction network maps a wiring diagram of cellular function. *Science* *353*, aaf1420.
- Cracan, V., Titov, D.V., Shen, H., Grabarek, Z., and Mootha, V.K. (2017). A genetically encoded tool for manipulation of NADP⁺/NADPH in living cells. *Nat. Chem. Biol.* *13*, 1088–1095.
- Dixon, S.J., Lemberg, K.M., Lamprecht, M.R., Skouta, R., Zaitsev, E.M., Gleason, C.E., Patel, D.N., Bauer, A.J., Cantley, A.M., Yang, W.S., et al. (2012). Ferroptosis: an iron-dependent form of nonapoptotic cell death. *Cell* *149*, 1060–1072.
- Doench, J.G., Fusi, N., Sullender, M., Hegde, M., Vaimberg, E.W., Donovan, K.F., Smith, I., Tothova, Z., Wilen, C., Orchard, R., et al. (2016). Optimized sgRNA design to maximize activity and minimize off-target effects of CRISPR-Cas9. *Nat. Biotechnol.* *34*, 184–191.
- Doll, S., Proneth, B., Tyurina, Y.Y., Panzilius, E., Kobayashi, S., Ingold, I., Irmiler, M., Beckers, J., Aichler, M., Walch, A., et al. (2017). ACSL4 dictates ferroptosis sensitivity by shaping cellular lipid composition. *Nat. Chem. Biol.* *13*, 91–98.
- Eaton, J.K., Furst, L., Ruberto, R.A., Moosmayer, D., Hillig, R.C., Hilpmann, A., Zimmermann, K., Ryan, M.J., Niehues, M., Badock, V., et al. (2018). Targeting a Therapy-Resistant Cancer Cell State Using Masked Electrophiles as GPX4 Inhibitors. *bioRxiv*.
- Fonseca, B.D., Zakaria, C., Jia, J.J., Graber, T.E., Svitkin, Y., Tahmasebi, S., Healy, D., Hoang, H.D., Jensen, J.M., Diao, I.T., et al. (2015). La-related Protein 1 (LARP1) Represses Terminal Oligopyrimidine (TOP) mRNA Translation Downstream of mTOR Complex 1 (mTORC1). *J. Biol. Chem.* *290*, 15996–16020.
- Frazier, A.E., Thorburn, D.R., and Compton, A.G. (2019). Mitochondrial energy generation disorders: genes, mechanisms and clues to pathology. *J. Biol. Chem.* *294*, 5386–5395. Published online December 12, 2017.
- Gao, M., Yi, J., Zhu, J., Minikes, A.M., Monian, P., Thompson, C.B., and Jiang, X. (2019). Role of Mitochondria in Ferroptosis. *Mol. Cell* *73*, 354–363.e3. Published online December 20, 2018.
- Gaude, E., Schmidt, C., Gammage, P.A., Dugourd, A., Blacker, T., Chew, S.P., Saez-Rodriguez, J., O'Neill, J.S., Szabadkai, G., Minczuk, M., et al. (2018). NADH Shuttling Couples Cytosolic Reductive Carboxylation of Glutamine with Glycolysis in Cells with Mitochondrial Dysfunction. *Mol. Cell* *69*, 581–593.e7.
- Gopal, R.K., Calvo, S.E., Shih, A.R., Chaves, F.L., McGuone, D., Mick, E., Pierce, K.A., Li, Y., Garofalo, A., Van Allen, E.M., et al. (2018a). Early loss of mitochondrial complex I and rewiring of glutathione metabolism in renal oncocyoma. *Proc. Natl. Acad. Sci. USA* *115*, E6283–E6290.
- Gopal, R.K., Kubler, K., Calvo, S.E., Polak, P., Livitz, D., Rosebrock, D., Sadow, P.M., Campbell, B., Donovan, S.E., Amin, S., et al. (2018b). Widespread Chromosomal Losses and Mitochondrial DNA Alterations as Genetic Drivers in Hurtle Cell Carcinoma. *Cancer Cell* *34*, 242–255.e245.
- Hangauer, M.J., Viswanathan, V.S., Ryan, M.J., Bole, D., Eaton, J.K., Matov, A., Galeas, J., Dhruv, H.D., Berens, M.E., Schreiber, S.L., et al. (2017). Drug-tolerant persister cancer cells are vulnerable to GPX4 inhibition. *Nature* *551*, 247–250.
- Hart, T., Chandrashekhar, M., Aregger, M., Steinhart, Z., Brown, K.R., MacLeod, G., Mis, M., Zimmermann, M., Fradet-Turcotte, A., Sun, S., et al. (2015). High-Resolution CRISPR Screens Reveal Fitness Genes and Genotype-Specific Cancer Liabilities. *Cell* *163*, 1515–1526.
- Hillenmeyer, M.E., Fung, E., Wildenhain, J., Pierce, S.E., Hoon, S., Lee, W., Proctor, M., St Onge, R.P., Tyers, M., Koller, D., et al. (2008). The chemical genomic portrait of yeast: uncovering a phenotype for all genes. *Science* *320*, 362–365.
- Hoppins, S., Collins, S.R., Cassidy-Stone, A., Hummel, E., Devay, R.M., Lackner, L.L., Westermann, B., Schuldiner, M., Weissman, J.S., and Nunnari, J. (2011). A mitochondrial-focused genetic interaction map reveals a scaffold-like complex required for inner membrane organization in mitochondria. *J. Cell Biol.* *195*, 323–340.
- Huang, S.H., and Lin, Y.W. (2018). Bioenergetic Health Assessment of a Single *Caenorhabditis elegans* from Postembryonic Development to Aging Stages via Monitoring Changes in the Oxygen Consumption Rate within a Microfluidic Device. *Sensors (Basel)* *18*, E2453.
- Huang da, W., Sherman, B.T., and Lempicki, R.A. (2009). Systematic and integrative analysis of large gene lists using DAVID bioinformatics resources. *Nat. Protoc.* *4*, 44–57.
- Ingold, I., Berndt, C., Schmitt, S., Doll, S., Poschmann, G., Buday, K., Roveri, A., Peng, X., Porto Freitas, F., Seibt, T., et al. (2018). Selenium Utilization by GPX4 Is Required to Prevent Hydroperoxide-Induced Ferroptosis. *Cell* *172*, 409–422.e21.
- Jain, I.H., Zazzeron, L., Goli, R., Alexa, K., Schatzman-Bone, S., Dhillon, H., Goldberger, O., Peng, J., Shalem, O., Sanjana, N.E., et al. (2016). Hypoxia as a therapy for mitochondrial disease. *Science* *352*, 54–61.
- Janos, L., and Korona, R. (2007). Epistatic buffering of fitness loss in yeast double deletion strains. *Nat. Genet.* *39*, 550–554.
- Kenwood, B.M., Weaver, J.L., Bajwa, A., Poon, I.K., Byrne, F.L., Murrow, B.A., Calderone, J.A., Huang, L., Divakaruni, A.S., Tomsig, J.L., et al. (2014). Identification of a novel mitochondrial uncoupler that does not depolarize the plasma membrane. *Mol. Metab.* *3*, 114–123. Published online November 28, 2013.
- Kershaw, C.J., Costello, J.L., Castelli, L.M., Talavera, D., Rowe, W., Sims, P.F., Ashe, M.P., Hubbard, S.J., Pavitt, G.D., and Grant, C.M. (2015). The yeast La related protein Slf1p is a key activator of translation during the oxidative stress response. *PLoS Genet.* *11*, e1004903.
- Khutornenko, A.A., Roudko, V.V., Chernyak, B.V., Vartapetian, A.B., Chumakov, P.M., and Evstafieva, A.G. (2010). Pyrimidine biosynthesis links mitochondrial respiration to the p53 pathway. *Proc. Natl. Acad. Sci. USA* *107*, 12828–12833.
- King, M.P., and Attardi, G. (1989). Human cells lacking mtDNA: repopulation with exogenous mitochondria by complementation. *Science* *246*, 500–503.
- Kühl, I., Miranda, M., Atanassov, I., Kuznetsova, I., Hinze, Y., Mourier, A., Filipovska, A., and Larsson, N.G. (2017). Transcriptomic and proteomic landscape of mitochondrial dysfunction reveals secondary coenzyme Q deficiency in mammals. *eLife* *6*, e30952.
- Lee, J.H., Liu, R., Li, J., Zhang, C., Wang, Y., Cai, Q., Qian, X., Xia, Y., Zheng, Y., Piao, Y., et al. (2017). Stabilization of phosphofructokinase 1 platelet isoform by AKT promotes tumorigenesis. *Nat. Commun.* *8*, 949.
- Li, W., Xu, H., Xiao, T., Cong, L., Love, M.I., Zhang, F., Irizarry, R.A., Liu, J.S., Brown, M., and Liu, X.S. (2014). MAGECK enables robust identification of essential genes from genome-scale CRISPR/Cas9 knockout screens. *Genome Biol.* *15*, 554.
- Liang, H., Yoo, S.E., Na, R., Walter, C.A., Richardson, A., and Ran, Q. (2009). Short form glutathione peroxidase 4 is the essential isoform required for survival and somatic mitochondrial functions. *J. Biol. Chem.* *284*, 30836–30844.
- Long, C.P., Gonzalez, J.E., Feist, A.M., Palsson, B.O., and Antoniewicz, M.R. (2018). Dissecting the genetic and metabolic mechanisms of adaptation to the knockout of a major metabolic enzyme in *Escherichia coli*. *Proc. Natl. Acad. Sci. USA* *115*, 222–227.
- Lu, W., Wang, L., Chen, L., Hui, S., and Rabinowitz, J.D. (2018). Extraction and Quantitation of Nicotinamide Adenine Dinucleotide Redox Cofactors. *Antioxid. Redox Signal.* *28*, 167–179.
- Madiraju, A.K., Erion, D.M., Rahimi, Y., Zhang, X.M., Braddock, D.T., Albright, R.A., Prigaro, B.J., Wood, J.L., Bhanot, S., MacDonald, M.J., et al. (2014). Metformin suppresses gluconeogenesis by inhibiting mitochondrial glycerophosphate dehydrogenase. *Nature* *510*, 542–546.
- Maiorino, M., Chu, F.F., Ursini, F., Davies, K.J., Doroshov, J.H., and Esworthy, R.S. (1991). Phospholipid hydroperoxide glutathione peroxidase is the 18-kDa selenoprotein expressed in human tumor cell lines. *J. Biol. Chem.* *266*, 7728–7732.

- Maiorino, M., Conrad, M., and Ursini, F. (2018). GPx4, Lipid Peroxidation, and Cell Death: Discoveries, Rediscoveries, and Open Issues. *Antioxid. Redox Signal.* *29*, 61–74.
- Meyers, R.M., Bryan, J.G., McFarland, J.M., Weir, B.A., Sizemore, A.E., Xu, H., Dharia, N.V., Montgomery, P.G., Cowley, G.S., Pantel, S., et al. (2017). Computational correction of copy number effect improves specificity of CRISPR-Cas9 essentiality screens in cancer cells. *Nat. Genet.* *49*, 1779–1784.
- Mootha, V.K., Lindgren, C.M., Eriksson, K.F., Subramanian, A., Sihag, S., Lehar, J., Puigserver, P., Carlsson, E., Ridderstråle, M., Laurila, E., et al. (2003). PGC-1 α -responsive genes involved in oxidative phosphorylation are coordinately downregulated in human diabetes. *Nat. Genet.* *34*, 267–273.
- Mootha, V.K., Handschin, C., Arlow, D., Xie, X., St Pierre, J., Sihag, S., Yang, W., Altshuler, D., Puigserver, P., Patterson, N., et al. (2004). Erralpha and Gabpa/b specify PGC-1 α -dependent oxidative phosphorylation gene expression that is altered in diabetic muscle. *Proc. Natl. Acad. Sci. USA* *101*, 6570–6575.
- Mor, I., Cheung, E.C., and Vousden, K.H. (2011). Control of glycolysis through regulation of PFK1: old friends and recent additions. *Cold Spring Harb. Symp. Quant. Biol.* *76*, 211–216.
- Morais, R., Gregoire, M., Jeannotte, L., and Gravel, D. (1980). Chick embryo cells rendered respiration-deficient by chloramphenicol and ethidium bromide are auxotrophic for pyrimidines. *Biochem. Biophys. Res. Commun.* *94*, 71–77.
- Mullen, A.R., Wheaton, W.W., Jin, E.S., Chen, P.H., Sullivan, L.B., Cheng, T., Yang, Y., Linehan, W.M., Chandel, N.S., and DeBerardinis, R.J. (2011). Reductive carboxylation supports growth in tumour cells with defective mitochondria. *Nature* *481*, 385–388.
- Mullen, A.R., Hu, Z., Shi, X., Jiang, L., Boroughs, L.K., Kovacs, Z., Boriack, R., Rakheja, D., Sullivan, L.B., Linehan, W.M., et al. (2014). Oxidation of alpha-ketoglutarate is required for reductive carboxylation in cancer cells with mitochondrial defects. *Cell Rep.* *7*, 1679–1690.
- Owen, M.R., Doran, E., and Halestrap, A.P. (2000). Evidence that metformin exerts its anti-diabetic effects through inhibition of complex 1 of the mitochondrial respiratory chain. *Biochem. J.* *348*, 607–614.
- Pagliarini, D.J., Calvo, S.E., Chang, B., Sheth, S.A., Vafai, S.B., Ong, S.E., Walford, G.A., Sugiana, C., Boneh, A., Chen, W.K., et al. (2008). A mitochondrial protein compendium elucidates complex I disease biology. *Cell* *134*, 112–123.
- Phang, J.M., Liu, W., Hancock, C.N., and Fischer, J.W. (2015). Proline metabolism and cancer: emerging links to glutamine and collagen. *Curr. Opin. Clin. Nutr. Metab. Care* *18*, 71–77.
- Piccioni, F., Younger, S.T., and Root, D.E. (2018). Pooled Lentiviral-Delivery Genetic Screens. *Curr Protoc Mol Biol.* *121*, 32.1.1–32.1.21.
- Robb, E.L., Hall, A.R., Prime, T.A., Eaton, S., Szibor, M., Viscomi, C., James, A.M., and Murphy, M.P. (2018). Control of mitochondrial superoxide production by reverse electron transport at complex I. *J. Biol. Chem.* *293*, 9869–9879.
- Sanjana, N.E., Shalem, O., and Zhang, F. (2014). Improved vectors and genome-wide libraries for CRISPR screening. *Nat. Methods* *11*, 783–784.
- Savaskan, N.E., Ufer, C., Kühn, H., and Borchert, A. (2007). Molecular biology of glutathione peroxidase 4: from genomic structure to developmental expression and neural function. *Biol. Chem.* *388*, 1007–1017.
- Shaham, O., Slate, N.G., Goldberger, O., Xu, Q., Ramanathan, A., Souza, A.L., Clish, C.B., Sims, K.B., and Mootha, V.K. (2010). A plasma signature of human mitochondrial disease revealed through metabolic profiling of spent media from cultured muscle cells. *Proc. Natl. Acad. Sci. USA* *107*, 1571–1575.
- Shalem, O., Sanjana, N.E., Hartenian, E., Shi, X., Scott, D.A., Mikkelsen, T., Heckl, D., Ebert, B.L., Root, D.E., Doench, J.G., and Zhang, F. (2014). Genome-scale CRISPR-Cas9 knockout screening in human cells. *Science* *343*, 84–87.
- Slavoff, S.A., Mitchell, A.J., Schwaid, A.G., Cabili, M.N., Ma, J., Levin, J.Z., Karger, A.D., Budnik, B.A., Rinn, J.L., and Saghatelian, A. (2013). Peptidomic discovery of short open reading frame-encoded peptides in human cells. *Nat. Chem. Biol.* *9*, 59–64.
- Stebbins, C.E., Kaelin, W.G., Jr., and Pavletich, N.P. (1999). Structure of the VHL-ElonginC-ElonginB complex: implications for VHL tumor suppressor function. *Science* *284*, 455–461.
- Stockwell, B.R., Friedmann Angeli, J.P., Bayir, H., Bush, A.I., Conrad, M., Dixon, S.J., Fulda, S., Gascón, S., Hatzios, S.K., Kagan, V.E., et al. (2017). Ferroptosis: A Regulated Cell Death Nexus Linking Metabolism, Redox Biology, and Disease. *Cell* *171*, 273–285.
- Tanner, L.B., Goglia, A.G., Wei, M.H., Sehgal, T., Parsons, L.R., Park, J.O., White, E., Toettcher, J.E., and Rabinowitz, J.D. (2018). Four Key Steps Control Glycolytic Flux in Mammalian Cells. *Cell Syst.* *7*, 49–62.e8.
- Tcherkezian, J., Cargnello, M., Romeo, Y., Huttlin, E.L., Lavoie, G., Gygi, S.P., and Roux, P.P. (2014). Proteomic analysis of cap-dependent translation identifies LARP1 as a key regulator of 5'TOP mRNA translation. *Genes Dev.* *28*, 357–371.
- Thompson Legault, J., Strittmatter, L., Tardif, J., Sharma, R., Tremblay-Vailancourt, V., Aubut, C., Boucher, G., Clish, C.B., Cyr, D., Daneault, C., et al.; LSFC Consortium (2015). A Metabolic Signature of Mitochondrial Dysfunction Revealed through a Monogenic Form of Leigh Syndrome. *Cell Rep.* *13*, 981–989.
- Thoreen, C.C., Chantranupong, L., Keys, H.R., Wang, T., Gray, N.S., and Sabatini, D.M. (2012). A unifying model for mTORC1-mediated regulation of mRNA translation. *Nature* *485*, 109–113.
- Titov, D.V., Cracan, V., Goodman, R.P., Peng, J., Grabarek, Z., and Mootha, V.K. (2016). Complementation of mitochondrial electron transport chain by manipulation of the NAD⁺/NADH ratio. *Science* *352*, 231–235.
- Trounce, I., Byrne, E., and Marzuki, S. (1989). Decline in skeletal muscle mitochondrial respiratory chain function: possible factor in ageing. *Lancet* *1*, 637–639.
- Ursini, F., Maiorino, M., and Gregolin, C. (1985). The selenoenzyme phospholipid hydroperoxide glutathione peroxidase. *Biochim. Biophys. Acta* *839*, 62–70.
- Vafai, S.B., and Mootha, V.K. (2012). Mitochondrial disorders as windows into an ancient organelle. *Nature* *491*, 374–383.
- Veatch, J.R., McMurray, M.A., Nelson, Z.W., and Gottschling, D.E. (2009). Mitochondrial dysfunction leads to nuclear genome instability via an iron-sulfur cluster defect. *Cell* *137*, 1247–1258.
- Visanji, N.P., Wislet-Gendebien, S., Oschipok, L.W., Zhang, G., Aubert, I., Fraser, P.E., and Tandon, A. (2011). Effect of Ser-129 phosphorylation on interaction of α -synuclein with synaptic and cellular membranes. *J. Biol. Chem.* *286*, 35863–35873.
- Viswanathan, V.S., Ryan, M.J., Dhruv, H.D., Gill, S., Eichhoff, O.M., Seashore-Ludlow, B., Kaffenberger, S.D., Eaton, J.K., Shimada, K., Aguirre, A.J., et al. (2017). Dependency of a therapy-resistant state of cancer cells on a lipid peroxidase pathway. *Nature* *547*, 453–457.
- Wang, T., Wei, J.J., Sabatini, D.M., and Lander, E.S. (2014). Genetic screens in human cells using the CRISPR-Cas9 system. *Science* *343*, 80–84.
- Wheaton, W.W., Weinberg, S.E., Hamanaka, R.B., Soberanes, S., Sullivan, L.B., Anso, E., Glasauer, A., Dufour, E., Mutlu, G.M., Budigner, G.S., and Chandel, N.S. (2014). Metformin inhibits mitochondrial complex I of cancer cells to reduce tumorigenesis. *eLife* *3*, e02242.
- Wise, D.R., Ward, P.S., Shay, J.E., Cross, J.R., Gruber, J.J., Sachdeva, U.M., Platt, J.M., DeMatteo, R.G., Simon, M.C., and Thompson, C.B. (2011). Hypoxia promotes isocitrate dehydrogenase-dependent carboxylation of α -ketoglutarate to citrate to support cell growth and viability. *Proc. Natl. Acad. Sci. USA* *108*, 19611–19616.
- Yang, W.S., SriRamaratnam, R., Welsch, M.E., Shimada, K., Skouta, R., Viswanathan, V.S., Cheah, J.H., Clemons, P.A., Shamji, A.F., Clish, C.B., et al. (2014). Regulation of ferroptotic cancer cell death by GPX4. *Cell* *156*, 317–331.

- Yeh, P.J., Hegreness, M.J., Aiden, A.P., and Kishony, R. (2009). Drug interactions and the evolution of antibiotic resistance. *Nat. Rev. Microbiol.* *7*, 460–466.
- Zahn, J.M., Poosala, S., Owen, A.B., Ingram, D.K., Lustig, A., Carter, A., Weeraratna, A.T., Taub, D.D., Gorospe, M., Mazan-Mamczarz, K., et al. (2007). AGEMAP: a gene expression database for aging in mice. *PLoS Genet.* *3*, e201.
- Zhang, Y., Chen, Y., Gucek, M., and Xu, H. (2016). The mitochondrial outer membrane protein MDI promotes local protein synthesis and mtDNA replication. *EMBO J.* *35*, 1045–1057.
- Zou, Y., Palte, M.J., Deik, A.A., Li, H., Eaton, J.K., Wang, W., Tseng, Y.Y., Deasy, R., Kost-Alimova, M., Dančák, V., et al. (2019). A GPX4-dependent cancer cell state underlies the clear-cell morphology and confers sensitivity to ferroptosis. *Nat. Commun.* *10*, 1617.

STAR★METHODS

KEY RESOURCES TABLE

REAGENT or RESOURCE	SOURCE	IDENTIFIER
Antibodies		
GPX4	Abcam	Cat # ab125066; RRID: AB_10973901
Beta-Actin	Sigma	Cat # A5441; RRID: AB_476744
ATP5B	Sigma	Cat # HPA001528; RRID: AB_1078242
TOMM20	Santa Cruz	Cat # SC-11415; RRID: AB_2207533
MT-CO1	Abcam	Cat # ab14705; RRID: AB_2084810
CYCS	BD Biosciences	Cat # 556432; RRID: AB_396416
Human OXPHOS cocktail	Abcam	Cat # ab110411; RRID: AB_2756818
LARP1	Abcam	Cat # ab86359; RRID: AB_1925169
FLAG M2	Sigma	Cat # F1804; RRID: AB_262044
PFKP	Sigma	Cat # HPA018257; RRID: AB_10960391
G6PD	Sigma	Cat # HPA000834; RRID: AB_1078977
HRP-linked anti-rabbit IgG	GE Healthcare	Cat # NA934; RRID: AB_772206
HRP-linked anti-mouse IgG	GE Healthcare	Cat # NXA931; RRID: AB_772209
IRDye 800CW Goat anti-Mouse IgG (H + L)	LI-COR Biosciences	Cat # 926-32210; RRID: AB_621842
IRDye 800CW Goat anti-Rabbit IgG (H + L)	LI-COR Biosciences	Cat # 926-32211; RRID: AB_621843
IRDye 680RD Goat anti-Mouse IgG (H + L)	LI-COR Biosciences	Cat # 926-68070; RRID: AB_10956588
IRDye 680RD Goat anti-Rabbit IgG (H + L)	LI-COR Biosciences	Cat # 926-68071; RRID: AB_10956166
Chemicals, Peptides, and Recombinant Proteins		
JKE-1674	Eaton et al., 2018	https://doi.org/10.1101/376764
DMEM, high glucose, pyruvate	GIBCO	Cat # 11995073
Sodium Pyruvate	GIBCO	Cat # 11360070
L-Glutamine	GIBCO	Cat # 25030081
Fetal Bovine Serum	GIBCO	Cat # 26140079
Fetal Bovine Serum, dialyzed	GIBCO	Cat # 26400044
DMEM, no glucose, no glutamine, no phenol red	GIBCO	Cat # A1443001
DMEM low Glucose, w/ L-Glutamine	US Biological	Cat # D9800
Seahorse XF Base Medium with 5 mM HEPES	Agilent	Cat # 103575-100
Phenol Red	Sigma	Cat # P3532
D-(+)-Glucose solution	Sigma	Cat # G8644
Galactose	Sigma	Cat # PHR1206
Uridine	Sigma	Cat # U3750
Penicillin-Streptomycin	GIBCO	Cat # 15140122
Puromycin Dihydrochloride	GIBCO	Cat # 10131035
G-418 solution	Sigma	Cat # 4727878001
Cell-Tak	Corning	Cat # 354240
Metformin / 1,1-Dimethylbiguanide HCl	Sigma	Cat # D150959
Piericidin A	Enzo Life Sciences	Cat # ALX-380-235-M002
Antimycin A	Sigma	Cat # A8674
Oligomycin A	Sigma	Cat # 75351
Ethidium bromide	Sigma	Cat # E1510
Chloramphenicol-Water Soluble	Sigma	Cat # C3175
Rotenone	Sigma	Cat # R8875
2-Deoxy-D-glucose	Sigma	Cat # D8375

(Continued on next page)

Continued

REAGENT or RESOURCE	SOURCE	IDENTIFIER
Carbonyl cyanide 3-chlorophenylhydrazone	Sigma	Cat # C2759
BAM15	Sigma	Cat # SML1760
ML 210	Sigma	Cat # SML0521
(±)- α -Tocopherol	Sigma	Cat # T3251
Ferrostatin-1	Sigma	Cat # SML0583
zVAD-fmk	Sigma	Cat # 219007
N-Acetyl-L-cysteine	Sigma	Cat # A9165
Sodium L-ascorbate	Sigma	Cat # A7631
Dimethyl succinate	Combi-Blocks	Cat # QE-5973
S1QEL1.1	Sigma	Cat # SML1948
MitoTEMPO	Sigma	Cat # SML0737
Mn(III)TBAP	Cayman Chemical	Cat # 75850
L-Glutathione reduced	Sigma	Cat # G4251
L-Glutathione oxidized	Sigma	Cat # G4376
Ammonium bicarbonate	Sigma	Cat # 09830
Ammonium carbonate	Fluka	Cat # 74415
Ammonium hydroxide	EMD Millipore	Cat # 533003
LC-MS grade water	Fisher Scientific	Cat # W64
NAD ⁺	Sigma	Cat # N0632
NADH	Sigma	Cat # N8129
¹³ C ₅ NAD ⁺	Toronto research chemicals	Cat # N407782
d5-NADH	Toronto research chemicals	Cat # N201487
Ammonium acetate	Sigma	Cat # 14267
Acetonitrile	Fisher Scientific	Cat # A955
XBridge BEH Amide column	Water	Cat # 186006091
ZIC-philic column	Merck	Cat # 150460
L-Glutamine 13C5, 99%	Cambridge Isotope Laboratories	Cat # CLM-1822-H-0.5
TWEEN 20	Sigma	Cat # P9416
Odyssey Blocking Buffer	LI-COR Biosciences	Cat # 927-40000
Dulbecco's PBS	Sigma	Cat # D8537
HBSS	GIBCO	Cat # 14025076
Critical Commercial Assays		
Seahorse XFe96 FluxPaks	Agilent	Cat # 102416-100
Seahorse XF Glycolytic Rate Assay Kit	Agilent	Cat # 103344-100
Annexin V Alexa Fluor 647 conjugate	Invitrogen	Cat # A23204
TMRM	Invitrogen	Cat # T668
Hoechst 33342, Trihydrochloride, Trihydrate	Invitrogen	Cat # H3570
BODIPY 581/591 C11	Invitrogen	Cat # D3861
MitoSOX Red	Invitrogen	Cat # M36008
TaqMan Gene Expression Master Mix	Applied Biosystems	Cat # 4369016
TaqMan <i>MT-ND1</i>	Thermo Fisher Scientific	Assay ID Hs02596873_s1
TaqMan <i>MT-ND2</i>	Thermo Fisher Scientific	Assay ID Hs02596874_g1
TaqMan <i>MT-CO1</i>	Thermo Fisher Scientific	Assay ID Hs02596864_g1
TaqMan <i>MT-CO2</i>	Thermo Fisher Scientific	Assay ID Hs02596865_g1
TaqMan <i>MT-CO3</i>	Thermo Fisher Scientific	Assay ID Hs02596866_g1
TaqMan <i>NDUFB8</i>	Thermo Fisher Scientific	Assay ID Hs00428204_m1
TaqMan <i>UQCRC2</i>	Thermo Fisher Scientific	Assay ID Hs00996395_m1

(Continued on next page)

Continued

REAGENT or RESOURCE	SOURCE	IDENTIFIER
TaqMan <i>TBP</i>	Thermo Fisher Scientific	Assay ID Hs00427620_m1
Novex 4–20% Tris-Glycine Mini Gels	Thermo Fisher Scientific	Cat # XP04202BOX
Trans-Blot Turbo Midi Nitrocellulose Transfer Packs	BioRad	Cat # 1704159
M-MLV Reverse Transcriptase	Promega	Cat # M1701
Deposited Data		
Expression levels in K562 based on RNaseq	Slavoff et al., 2013	GEO: GSE34740
Experimental Models: Cell Lines		
K562	ATCC	CCL-243
HeLa	ATCC	CCL-2
293T	ATCC	CRL-3216
A375	ATCC	CRL-1619
HT-29	ATCC	HTB-38
HAP1	Horizon Discovery	C631
HAP1 <i>GPX4</i> KO	Horizon Discovery	HZGHC005981c005
HAP1 <i>NDUFA9</i> KO	Horizon Discovery	HZGHC002487c004
Oligonucleotides		
GFP sgRNA control GGGCGAGGAGCTGTTCACCG	This paper	N/A
G6PD sgRNA 1 AGAGGTGCAGCCAACAATG	This paper	N/A
G6PD sgRNA 2 TGCCCGTTCCCGCCTCACAG	This paper	N/A
PFKP sgRNA 1 GATGTGTGTCAAACCTCTCGG	This paper	N/A
PFKP sgRNA 2 GCCGGATGATCAGATCCCAA	This paper	N/A
GPX4 sgRNA 1 AGAGATCAAAGAGTTCGCCG	This paper	N/A
GPX4 sgRNA 2 GAGCTGAGTGTAGTTACTT	This paper	N/A
LARP1 sgRNA 1 TAGTGAATACTACTTCAGCG	This paper	N/A
LARP1 sgRNA 2 GCTGTTCTAAACAGCGCAA	This paper	N/A
REXO2 sgRNA 1 CTTGCAGTCTGGCCTTACCA	This paper	N/A
REXO2 sgRNA 2 ATAATCAGGTTAGGACCCTG	This paper	N/A
Taqman mtDNA assay-ND2 Forward TGTTGGTTAT ACCCTTCCCGTACTA	Bao et al., 2016	https://doi.org/10.7554/eLife.10575
Taqman mtDNA assay-ND2 Reverse CCTGCAAAGA TGGTAGAGTAGATGA	Bao et al., 2016	https://doi.org/10.7554/eLife.10575
Taqman mtDNA assay-ND2 Probe ccctggcccaaccc	Bao et al., 2016	https://doi.org/10.7554/eLife.10575
Taqman nucDNA assay- AluYb8 Forward CTTGCAG TGAGCCGAGATT	Bao et al., 2016	https://doi.org/10.7554/eLife.10575
Taqman nucDNA assay- AluYb8 Reverse GAGACG GAGTCTCGCTCTGTC	Bao et al., 2016	https://doi.org/10.7554/eLife.10575
Taqman nucDNA assay- AluYb8 Probe ACTGCAG TCCGAGTCCGGCCT	Bao et al., 2016	https://doi.org/10.7554/eLife.10575
Recombinant DNA		
lentiCRISPR v2	Addgene	Plasmid # 52961
psPAX2	Addgene	Plasmid # 12260
pMD2.G	Addgene	Plasmid # 12259
pWPI /Neo	Addgene	Plasmid # 35385
pWPI/ IGPX4 / Neo	This paper	N/A
pWPI/ sGPX4 / Neo	This paper	N/A
pWPI/ TPNOX-FLAG / Neo	This paper	N/A

(Continued on next page)

Continued

REAGENT or RESOURCE	SOURCE	IDENTIFIER
Software and Algorithms		
MATLAB	MathWorks	https://www.mathworks.com/products/matlab.html
Jupyter	Project Jupyter	https://jupyter.org
R	The R Foundation	http://www.R-project.org
ImageJ	NIH	https://imagej.nih.gov/ij/
Seahorse Wave Desktop Software	Agilent	https://www.agilent.com/en/products/cell-analysis/cell-analysis-software/data-analysis/wave-desktop-2-6
Compound Discoverer Software	Thermo Fisher Scientific	https://www.thermofisher.com/us/en/home/industrial/mass-spectrometry/liquid-chromatography-mass-spectrometry-lc-ms/lc-ms-software/multi-omics-data-analysis/compound-discoverer-software.html
Prism	GraphPad	https://www.graphpad.com/scientific-software/prism/
FlowJo	BD	https://www.flowjo.com
MAGeCK	Li et al., 2014	https://sourceforge.net/p/mageck/wiki/Home/
Gene set enrichment analysis (GSEA)	Broad Institute	http://software.broadinstitute.org/gsea/index.jsp
MATLAB code for computing Z and ΔZ scores	This paper	https://github.com/yangli88
Python code for computing p values and FDRs	This paper	https://github.com/yangli88

LEAD CONTACT AND MATERIALS AVAILABILITY

Further information and requests for resources and reagents should be directed to and will be fulfilled by the Lead Contact, Vamsi K. Mootha (vamsi@hms.harvard.edu).

EXPERIMENTAL MODEL AND SUBJECT DETAILS**Cell Lines**

K562 (ATCC CCL-243), HeLa (ATCC CCL-2), 293T (ATCC CRL-3216), A375 (ATCC CRL-1619) and HT-29 (ATCC No. HTB-38) cells were obtained from ATCC. All experiments with wild-type cells or CRISPR-Cas9 mediated knockouts were performed under passage number 20 upon receipt from ATCC, and late passage cells were authenticated by STR profiling. HAP1 wild-type cells and gene-specific knockouts were obtained from Horizon Discovery and were authenticated by genomic PCR and sequencing.

METHOD DETAILS**Determination of Infection Conditions for CRISPR Pooled Screens**

Optimal infection conditions were determined in order to achieve 30%–50% infection efficiency, corresponding to a multiplicity of infection (MOI) of ~0.5–1. Spin-infections were performed in 12-well plate format with 3×10^6 cells each well. Optimal conditions were determined by infecting cells with different virus volumes (0, 100, 200, 400, 600, 800 μ L) with a final concentration of 4 μ g/mL polybrene in K562 cells. Cells were centrifuged for 2 h at 930xg at 30°C. Approximately 24 h after infection, cells were collected and 4×10^5 K562 cells from each infection were seeded in 2 wells of a 6-well plate, each with complete medium, one supplemented with the appropriate concentration of puromycin. Cells were counted 2 days post selection to determine the infection efficiency, comparing survival with and without puromycin selection. Volume of virus that yielded ~30%–50% infection efficiency was used for screening.

Genome Scale CRISPR Screens with Brunello All-in-one Library

Brunello barcoded all-in-one library contains 77,441 sgRNA, which includes an average of 4 guides per gene and 1000 non-targeting control guides. Infection, selection and expansion were performed in three distinct replicates. Screening-scale infections were

performed with the pre-determined volume of virus in the same 12-well format as the viral titration described above, and pooled 24 h post-centrifugation. Infections were performed with $\sim 1.5 \times 10^8$ cells per replicate, in order to achieve a representation of at least 500 cells per sgRNA following puromycin selection ($\sim 4 \times 10^7$ surviving cells). Approximately 24 h after infection, all wells within a replicate were pooled and were split into T225 flasks. 48 h after infection, cells were selected with puromycin for 4-5 days to remove uninfected cells. After selection was complete, at least 4×10^7 of K562 cells were seeded in T225 flasks. Media with 10 mM Metformin, 10 nM Piericidin, 100 nM Antimycin, 10 nM Oligomycin, 10 nM Antimycin and 10 nM Oligomycin, 100 ng/mL Ethidium Bromide and 10 μ g/mL Chloramphenicol was then added to the cells. Cells were passaged in fresh media containing drugs every 2-3 days. Cells were harvested 15 days after initiation of treatment.

For all screens, genomic DNA (gDNA) was isolated using Maxi (3×10^7 – 1×10^8 cells) kits according to the manufacturer's protocol (QIAGEN). PCR and sequencing were performed as previously described (Doench et al., 2016; Piccioni et al., 2018). Samples were sequenced on a HiSeq2000 (Illumina). Of note, two of our "day 15 samples," one for DMSO and one for metformin, were lost during the PCR step, yielding a total of 22 (out of 24) successful 15 day screens (Table S2).

Gene-Specific CRISPR-Cas9 Knockouts

The two best sgRNAs from the Brunello-4 library were ordered as complementary oligonucleotides (Integrated DNA Technologies) and cloned into pLentiCRISPRv2. An sgRNA targeting EGFP was used as a negative control. Lentiviruses were produced according to Addgene's protocol (Sanjana et al., 2014) and cells were selected with 2 μ g/mL puromycin 24 h post-infection. Puromycin was withdrawn 48 h later and cells were maintained in for 10-20 additional days before analysis. Gene disruption efficiency was verified by protein immunoblotting. The sequences of the sgRNAs used are in the Key Resources Table.

Gene-Specific cDNA Rescue

SgRNA-resistant versions of sGPX4 and IGPX4 containing the 3' SECIS sequence were *in vitro* synthesized (Integrated DNA Technologies) to encode silent mutations within the GPX4 sgRNA recognition sites. The cDNAs were cloned into pWPI-Neo (Visanji et al., 2011) and lentiviruses were produced and selected according to Addgene's protocol. The sequences of sgRNA-resistant sGPX4 and IGPX4 are below, with lowercase letters denoting 3' UTR. The original recognition sites for GPX4 sgRNA that were silently mutated were underscored.

sGPX4

ATGTGCGCGTCCCGGGACGACTGGCGCTGTGCGCGCTCCATGCACGAGTTTTCCGCCAAGGACATCGACGGGCACATGGTTAA
 CCTGGACAAGTACCGGGGCTTCGTGTGCATCGTACCAACGTGGCCTCCCAGTGAGGCAAGACCGAAGTGAATTATACCCAACCTT
 GTCGACCTGCACGCCGATACGCTGAGTGTGGTTTTCGGATACTGGCCTTCCCCTGTAACCAGTTCGGGAAGCAGGAGCCAGG
 GAGTAACGAAGAAATAAGGAATTTGCAGCGGGCTACAACGTCAAATTCGATATGTTTCAGCAAGATCTGCGTGAACGGGGACGAC
 GCCCACCCGCTGTGGAAGTGGATGAAGATCCAACCCAAGGGCAAGGGCATCCTGGGAAATGCCATCAAGTGGAACTTCACCAA
 GTTCTCATCGACAAGAACGGCTGCGTGGTGAAGCGCTACGGACCCATGGAGGAGCCCCTGGTATAGAGAAGGACCTGCCCC
 ACTATTTCTAGctccacaagtgtgtggccccgcccagcccctgccacgcccttgagcctccaccggcactcatgacggcctgctgcaaaccgtctgtgtggggcag
 acccgaaaatccagcgtgcaccccgccggaggaaggtcccatggcctgctgggcttgctcggcgccccaccctggctacctgtggaataaacagacaaattagcctg
 ctgataaaaaaa

IGPX4

ATGAGCCTCGGCCGCTTTGCCGCTACTGAAGCCGGCGCTGCTCTGTGGGGCTCTGGCCGCGCCTGGCCTGGCCGGGACCT
 CTGCGCGTCCCGGGACGACTGGCGCTGTGCGCGCTCCATGCACGAGTTTTCCGCCAAGGACATCGACGGGCACATGGTTAAC
 CTGGACAAGTACCGGGGCTTCGTGTGCATCGTACCAACGTGGCCTCCCAGTGAGGCAAGACCGAAGTGAATTATACCCAACCTT
 GTCGACCTGCACGCCGATACGCTGAGTGTGGTTTTCGGATACTGGCCTTCCCCTGTAACCAGTTCGGGAAGCAGGAGCCAGG
 GAGTAACGAAGAAATAAGGAATTTGCAGCGGGCTACAACGTCAAATTCGATATGTTTCAGCAAGATCTGCGTGAACGGGGACGA
 CGCCACCCGCTGTGGAAGTGGATGAAGATCCAACCCAAGGGCAAGGGCATCCTGGGAAATGCCATCAAGTGGAACTTCACCAA
 GTTCTCATCGACAAGAACGGCTGCGTGGTGAAGCGCTACGGACCCATGGAGGAGCCCCTGGTATAGAGAAGGACCTGCCCC
 ACTATTTCTAGctccacaagtgtgtggccccgcccagcccctgccacgcccttgagcctccaccggcactcatgacggcctgctgcaaaccgtctgtgtggggcag
 acccgaaaatccagcgtgcaccccgccggaggaaggtcccatggcctgctgggcttgctcggcgccccaccctggctacctgtggaataaacagacaaattagcctg
 ctgataaaaaaa

TPNOX Expression

A short peptide (SGGSGG) for vector control or cytosolic TPNOX (Cracan et al., 2017) was cloned into pWPI-Neo (Visanji et al., 2011). Lentiviruses were produced and according to Addgene's protocol. The sequence of cytosolic TPNOX containing a C-terminal FLAG tag is below.

TPNOX

ATGAAGGTCACCGTGGTTCGGATGCACCCATGCCGGCACCTTCGCCATCAAGCAAATCCTCGCTGAGCACCTGACGCCGAGGT
 CACCGTCTACGAGAGGAACGATGTGATCTCCTTCTGTCTGTGGCATCGCCCTTACCTGGGCGGAAAAGTGGCCGATCCCCA
 AGGCCTCTTCTACAGCTCCCCTGAAGAACTGCAGAAGCTGGGCGCTAATGTGCAGATGAACCACAACGTGCTGGCCATCGACCC
 TGACCAAAAAGACCGTACAGTTCGAGGACCTACCAATCACGCCAGACCCGAGTCTACGACAACTGGTGTGACCTCCGG
 AAGCTGGCCTATCGTGCCAAAATCCCCGGCATCGACAGCGATAGGGTGAAGCTCTGCAAGAATTGGGCCACGCCAGGCTCT

GATTGAGGACGCCAAGGAGGCCAAGAGGATCACCGTCATCGGCGCCGGATACATCGCCGCCAACTGGCCGAGGCCTACTCC
 ACAACAGGCCACGACGTCACCCTGATTGCCAGAAGCGCTAGGGTCATGAGGAAGTACTTCGATGCCGACTTCACCGACGTCATC
 GAACAGGACTACAGGGACCATGGCGTGCAACTCGCTCTGGGCGAGACAGTGGAGAGCTTCACCGACAGCGCCACCGGCCTCA
 CAATCAAGACAGACAAGAACTCCTATGAGACCGACCTGGCCATCCTCTGCATTGGCTTTAGGCCAACACAGACCTGCTGAAAG
 GCAAAGTGGACATGGCCCCTAACGGCGCCATCATTACCGACGACTACATGAGGTCCAGCAACCCTGATATTTTCGCTGCTGGCG
 ACTCCGCGCCGTCATTACAACCCACACACCAAAACGCCTACATTCCTCGCTACCAACGCCGTCAGGCAGGGAATCCTC
 GTCGGAAAGAACCCTCGTCAAGCCCACAGTGAAGTACATGGGAACCCAGTCCAGCTCCGGACTGGCCCTCTATGACAGGACAATT
 GTCTCCACAGGCCTCACACTGGCCGCCGCAAGCAACAAGGCCTCAATGCCGAGCAGGTTCATCGTGGAGGACAACCTATAGGC
 CCGAGTTCATGCCTCCACCGAGCCCGTCTCATGAGCCTGGTCTTCGACCCCGATACACACAGAATCCTGGGAGGCGCCCT
 GATGTCCAAATACGACGTGTCCAGAGCGCTAATACCCTGTCCGTCTGCATCCAGAACGAGAACCACCATCGATGACCTGGCCA
 TGGTGGACATGCTGTTCCAGCCCAATTTTCGACAGGCCCTTCAACTACCTGAACATTCTCGCCAGGCTGCCCAAGCTAAAGTGGC
 CCAATCCGTCACGCTGGAGGCAGCGATTACAAGGATGACGATGACAAG

Cell Death Assay

Cells were treated with OXPPOS inhibitors and grown in glucose (10 mM) or galactose (10 mM) media for 24 h. Cell death was assessed by staining cells with Annexin V Alexa Fluor 647 conjugate (Invitrogen) according to the manufacturer's protocol. Alexa Fluor fluorescence was analyzed by flow cytometry on a BD Accuri C6 (BD Biosciences).

Oxygen Consumption by the Seahorse XF Analyzer

1.5×10^5 K562 cells were plated on a Seahorse plate coated with Cell-Tak (Corning) in DMEM containing 5.5 mM glucose (D9800 US Biological) supplemented with 4 mM glutamine (GIBCO). Oxygen consumption was recorded by a Seahorse XFe96 Analyzer (Agilent) using the mito stress test protocol, in which cells were sequentially perturbed by 2 μ M oligomycin, 2 μ M CCCP or 3 μ M BAM15, and 0.5 μ M piericidin + 0.5 μ M antimycin.

Glycolytic Rate Assay by the Seahorse XF Analyzer

1.5×10^5 K562, 5×10^4 HeLa, or 5×10^4 HAP1 cells were plated on a Seahorse plate coated with Cell-Tak (Corning) in Seahorse XF Base Medium with 5 mM HEPES (Agilent) supplemented with 25 mM glucose (Sigma), 1 mM pyruvate (GIBCO), and 4 mM glutamine (GIBCO). Extracellular acidification rate was recorded by a Seahorse XFe96 Analyzer (Agilent) using the glycolytic rate assay protocol, in which cells were sequentially perturbed by 0.5 μ M rotenone + 0.5 μ M antimycin and 50 mM 2-Deoxy-D-glucose. The extracellular acidification rate (ECAR) was corrected for contribution from mitochondrial respiration using oxygen consumption data using the Seahorse Wave Desktop Software (Agilent), such that acidification is due primarily to lactate excretion. The corrected extracellular acidification rate, termed GlycoPER, was used as a proxy for glycolytic flux.

Polyacrylamide Gel Electrophoresis and Protein Immunoblotting

Cells were harvested, washed in PBS and lysed for 5 min on ice in lysis buffer (50 mM Tris/HCl at pH 7.5, 150 mM NaCl, 1mM MgCl₂, 1% NP-40, protease / phosphatase inhibitors). Lysates were clarified by centrifugation for 5 min at 2,000xg. Gel electrophoresis was performed using Novex Tris-Glycine 4%–20% gels (Thermo Fisher Scientific). Semi-dry western blotting was performed using the Trans-Blot Turbo blotting system and PVDF membranes (BioRad). Immunoblotting was performed in 5% milk powder in PBS + 0.1% Tween-20 (Sigma) or in Odyssey Blocking Buffer (LI-COR Biosciences).

Quantification of mtDNA by Real-Time PCR

DNA was extracted from cells treated with OXPPOS inhibitors and analyzed by multiplex real-time quantitative PCR as described in (Bao et al., 2016). Custom-synthesized assays for the *AluYb8* repeat element (nuclear DNA) and *MT-ND2* (mitochondrial DNA) were obtained from Applied Biosystems.

Mitochondrial Membrane Potential Measurement

K562 cells were treated with OXPPOS inhibitors and grown for 3 days. One h prior to measurement, cells were concentrated to 10^6 cells/mL in phenol red-free media supplemented with OXPPOS inhibitors. TMRM (Invitrogen) was added to the cells at a final concentration of 10 nM. TMRM fluorescence was analyzed by confocal microscopy. In Figure S1E, cells were co-stained with Hoechst 33342 (Invitrogen) at a concentration of 0.5 μ g/mL, and imaged under a spinning disk (Yokogawa) confocal microscope (Zeiss) equipped with a CCD camera (Hamamatsu). Image processing was performed using the ImageJ software (NIH). Maximum projection was taken across Z stacks of 3 frames of view and the maximum intensity of each cell was recorded. In Figure S5C, at least 60 cells from 5 frames of view were analyzed for each treatment.

Growth Experiments

Follow-up for *GPX4* was performed in K562, HAP1, and HeLa cells. Follow-up for *NDUFA9* was performed in HAP1 cells. Follow-up for *G6PD* was performed in K562 and A375 cells. Follow-up for *PFKP* was performed in K562 and HT-29 cells. Follow-up for *LARP1* and *REXO2* was performed in K562 cells. Unless noted otherwise, cells were grown in DMEM (GIBCO) with 25 mM glucose (Sigma),

4 mM L-glutamine (GIBCO), 1 mM sodium pyruvate (GIBCO), 10% fetal bovine serum (GIBCO), 100U penicillin-100 μ g/mL streptomycin (GIBCO), and 50 μ g/mL uridine (Sigma).

For follow-up of *G6PD*, *PFKP*, *LARP1* and wild-type cells in K562, cells were seeded in triplicates at 2×10^5 /mL (~12.5% of maximum cell density) in 2 mL media in 12-well plates. For follow-up of *GPX4* and *REXO2* in K562, cells were seeded in triplicates at 5×10^4 /mL (~3% of maximum cell density) in 2 mL media in 12-well plates. Cell counts were performed 3 days after drug treatments. For follow-up in HAP1, HeLa and 293T, cells were seeded in triplicates at 5×10^4 per well (~10% confluency) in 2 mL media in 12-well plates. Counts were performed 3 days after plating. For follow-up in HT29 and A375, cells were seeded in triplicates at 1×10^5 per well (~20% confluency) in 2 mL media in 12-well plates. Counts were performed 3 days after plating. Population doubling was calculated as $\log_2(\text{final density}/\text{seeding density})$.

For spent media growth experiment in K562 (Figure 4B), cells were treated with DMSO or oligomycin and grown for 3 days. Media were harvested and clarified by centrifugation and vacuum filtering. The spent media were supplemented with fresh OXPPOS inhibitors during the growth experiments. Cells were seeded in triplicates at 5×10^4 /mL under spent media growth, as well as under fresh media growth in Figure S3B.

For cells infected with viruses carrying the pWPI lentivector, 500 μ g/mL or 800 μ g/mL of G-418 (Sigma) was used to select for stable lines in HAP1 and K562, respectively.

Lipid Peroxidation Measurement

Cells treated with various chemicals were harvested, washed with HBSS (GIBCO), and resuspended in HBSS to 0.5 mL, and incubated with 2 μ M BODIPY 581/591 C11 (Invitrogen) for 10 min at 37 °C. Cells were then washed twice in HBSS and analyzed by flow cytometry on a BD Accuri C6 (BD Biosciences). Quantification of BODIPY-C11 fluorescence was performed as described in (Dixon et al., 2012; Yang et al., 2014).

Mitochondrial Superoxide Measurement

Cells treated with various chemicals were harvested, washed with HBSS (GIBCO), and resuspended in HBSS to 0.5 mL, and incubated with 5 μ M MitoSOX Red (Invitrogen) for 10 min at 37 °C. Cells were then washed twice in HBSS and analyzed by flow cytometry on a BD Accuri C6 (BD Biosciences).

Isolation of Mitochondria

HAP1 cells were grown in 3-5 15 cm dishes until confluence. Cells were then harvested, washed in PBS, and washed once with 10 mL of MB buffer (210 mM mannitol, 70 mM sucrose, 10 mM HEPES-KOH at pH 7.4, 1mM EDTA, protease/phosphatase inhibitor). Cells were resuspended in 1 mL of MB buffer and transferred to 2 mL glass homogenizer (Kontes). Breaking of cells was achieved by pressing the potter (Kontes) up and down of the homogenizer about 35 times on ice. Treated cells were transferred to a 15 mL tube, with volume increased to 6 mL with MB buffer. The mixture was centrifuged at 2,000xg for 5 min and the pellet (nuclei and intact cells) was discarded. The supernatant, which contained the cytoplasm and mitochondria, was distributed to 1.5 mL Eppendorf tubes and centrifuged at 13,000xg for 10 min at 4°C. The supernatant contained the cytosolic fraction whereas the small, solid brown pellets contained the mitochondria. The cytosolic fraction was saved. The mitochondrial pellets were washed by MB buffer once, resuspended in MB buffer, and saved. Western blotting was performed on the cytosolic and mitochondrial fractions as described in the “Polyacrylamide gel electrophoresis and protein immunoblotting” section.

Immunofluorescence Experiment

HAP1 cells were seeded in 35-mm glass bottom dishes (MatTek) and grown until ~70% confluent. Cells were fixed with 10% formalin in PBS at room temperature for 30 min, washed 3X in PBS, and blocked with PBS + 0.1% Triton X-100 + 1% BSA for 2 h at room temperature. Cells were incubated with primary antibodies (1:250 anti-GPX4, 1:500 anti-CYCS) in PBS + 0.1% Triton X-100 + 1% BSA overnight at 4°C. Cells were washed 3X in PBS, and incubated with secondary antibodies (1:200) in PBS + 0.1% Triton X-100 + 1% BSA for 3 h at room temperature. Cells were then washed 3X in PBS, stained with 1:2000 Hoechst 33342 (Invitrogen) for 10 min at room temperature, and imaged under a spinning disk (Yokogawa) confocal microscope (Zeiss) equipped with a CCD camera (Hamamatsu). Image processing was performed using the ImageJ software (NIH).

Gene Expression Assay by Real-Time PCR

Real-time quantitative PCR was performed using the TaqMan technology (Applied Biosystems). Briefly, total RNA was extracted with the RNeasy kit (QIAGEN) and digested with DNase-I (QIAGEN). Reverse transcription was performed using MLV reverse transcriptase supplemented with RNasin and dNTP (Promega). Real-time qPCR was performed using the standard protocol for Taqman assay on a C1000 Touch thermal cycler (BioRad). All data were normalized to *TBP*. The Taqman probes used in this study are listed in the Key Resources Table.

Intracellular Metabolite Profiling using Liquid Chromatography-Mass Spectrometry (LCMS):

6×10^5 cells/well (K562) in 3 mL were seeded in 6-well plates in the presence of OXPPOS inhibitors. After 72 h, equal number of cells were centrifuged at 600xg for 5 min at room temperature and the media were aspirated off. For intracellular metabolite profiling, cells

were rinsed with 1 mL of PBS and metabolism was quenched by adding 1 mL of dry ice-cold 80% methanol. After incubation on ice for 20 min, the supernatant was collected after centrifugation of the sample at 21,000xg for 20 min at 4°C, dried in a speed vacuum concentrator (Savant SPD1010, Thermo Fisher Scientific), and stored at –80°C until the analysis. Metabolite extracts were resuspended in 100 µL of 60/40 acetonitrile/water, vortexed, and sonicated in ice-cold water for 1 min. The extracts were then incubated on ice for 20 min and clarified by centrifugation at 21,000xg for 20 min at 4°C. Next, 55 µL of supernatant was transferred to an autosampler vial and pooled QC sample was generated by combining around 20 µL of each sample.

Polar metabolite separation was done using Dionex Ultimate 3000 UHPLC system and ZIC-philic column (150x2.1 mm, 5 µm, Merck KGaA). Mobile phase A (MPA) was 20 mM ammonium carbonate in water, pH 9.6 (adjusted with ammonium hydroxide), and mobile phase B (MPB) was acetonitrile. The column was held at 27°C, injection volume 5 µL, and an autosampler temperature of 4°C. LC conditions at flow rate of 0.15 mL/min were: 0 min: 80% B, 0.5 min: 80% B, 20.5 min: 20% B, 21.3 min: 20% B, 21.5 min: 80% B with 7.5 min of column equilibration time. Mass spectrometry (MS) detection was performed using Q-Exactive plus Orbitrap mass spectrometer (Thermo Fisher Scientific) with an Ion Max source and HESI II probe operating in switch polarity mode. MS parameters were: sheath gas flow 30, aux gas flow 7, sweep gas flow 2, spray voltage 2.80 for negative & 3.80 for positive, capillary temperature 310°C, S-lens RF level 50 and aux gas heater temp 370°C. Data acquisition was done using Xcalibur 4.1 (Thermo Fisher Scientific) and performed in full scan mode with a range of 70-1000 m/z, resolution 70,000, AGC target 1×10^6 and maximum injection time of 80 ms. Data analysis was done using Compound Discoverer 3.0. Samples were injected in randomized order and pooled QC samples were injected regularly throughout the analytical batch. Metabolite annotation was done base on accurate mass (± 5 ppm) and matching retention time (± 0.3 min) as well as MS/MS fragmentation pattern from the pooled QC sample against in-house retention time+MSMS library of reference chemical standards. Metabolites which have CV < 20% in pooledQC, were used for the statistical analysis.

NADH/NAD⁺ Analysis using LCMS

After centrifugation and removal of media, samples were prepared as described in (Lu et al., 2018). In brief, cells were lysed with ice-cold 4/4/2 acetonitrile/methanol/water with 0.1 M formic acid containing ¹³C₅ NAD⁺ and d5-NADH internal standards, neutralized with 15% ammonium bicarbonate for 3 min, centrifuged at 21,000xg and 4°C, and injected 5 µL of supernatant on ZIC-philic column with above mentioned LC-MS parameters. Calibration curves of NAD⁺ and NADH were generated using ¹³C₅ NAD⁺ and d5-NADH internal standards.

Stable Isotope Analysis of [U-¹³C]glutamine

For K562 cells, 6×10^5 cells/well in 3 mL were seeded in 6-well plates in the presence of OXPPOS inhibitors and after 48 h, media in each plate were exchanged with isotope tracing media consisting of glutamine-free & uridine-free DMEM containing 25 mM glucose (Sigma), 1 mM sodium pyruvate (GIBCO), 10% dialyzed FBS (GIBCO), 100U penicillin-100 µg/mL streptomycin (GIBCO), and supplemented with 2 mM [U-¹³C]Glutamine. After 8 h of incubation, equal numbers of cells were centrifuged, media were aspirated off, and 1 mL of dry ice-cold 80% methanol was added to extract metabolite and incubated on ice for 20 min. Next, intracellular metabolite profiling was performed as described previously.

HAP1, HT29, and 293T cells were seeded in 6 well-plates at 10^6 cells per well and grown overnight. On the next day, media in each plate were exchanged as described previously with OXPPOS inhibitors. After 8 h of incubation, media were aspirated off and tracer analysis was performed as described above. Natural abundance correction was performed using Stable Isotope labeling workflow within Compound Discoverer 3.0 (Thermo Fisher Scientific).

Media Lactate Analysis

After 3 days of cell growth, 30 µL of media were extracted with 120 µL of ice-cold acetonitrile, incubated on ice for 20 min, centrifuged at 21,000xg for 20 min at 4°C, and supernatant was transferred to an autosampler vial. Media metabolite separation was done using XBridge BEH amide (2.1x100mm, 2.5 µm, Waters Corporation) column on Dionex Ultimate 3000 UHPLC system. MPA was 5/95 acetonitrile/water, 20 mM ammonium acetate, pH 9.0 and MPB was acetonitrile. The column was held at 27°C, injection volume 10 µL, autosampler temperature 4°C. LC conditions at flow rate of 0.22 mL/min were: 0 min: 85% B, 0.5 min: 85% B, 9.00 min: 35% B, 11 min: 2% B, 12 min: 2% B, 13.5 min: 85% B with 4.5 min of column equilibration time. Mass spectrometry (MS) detection was performed using Q-Exactive plus Orbitrap mass spectrometer (Thermo Fisher Scientific) with an Ion Max source and HESI II probe operating in switch polarity mode. MS parameters were: sheath gas flow 50, aux gas flow 10, sweep gas flow 2, spray voltage 2.50 for negative & 3.80 for positive, capillary temperature 310°C, S-lens RF level 50 and aux gas heater temp 370°C. Data acquisition was done using Xcalibur 4.1 (Thermo Fisher Scientific) and performed in full scan mode with a range of 70-1000 m/z, resolution of 70,000, AGC target of 3×10^6 , and maximum injection time of 80 ms. Data analysis was done as described previously.

QUANTIFICATION AND STATISTICAL ANALYSIS

Gene Scoring

Raw sgRNA read counts were normalized to reads per million and then log₂ transformed using the following formula:

$$\text{Log}_2(\text{Reads from an individual sgRNA} / \text{Total reads in the sample} * 10^6 + 1)$$

Log2 fold-change of each sgRNA was determined relative to the initial time point (day 0). The replicates were paired throughout the course of the screens.

For each gene in each replicate, the mean log2 fold-change in the abundance of all 4 sgRNAs was calculated. Genes with low expression ($\log_2 \text{FPKM} < 0$) according to publicly available K562 RNA-seq dataset (sample GSM854403 in GEO series GSE34740) were removed. This step filtered out about 50% of all genes, leading to a gene set of 11,102 genes for further analysis. Log2 fold-changes were averaged by taking the mean across replicates. For each treatment, a null distribution was defined by the 3,726 genes with lowest expression ($\log_2 \text{FPKM} = -7$). We chose non-expressing genes instead of non-targeting guides for the null distributions since we observed a systematic, significant enrichment of non-targeting guides (Figure S1G) at the late time point. To score each gene within each treatment, its mean log2 fold-change across replicates was Z-score transformed, using the statistics of the null distribution defined as above. The normalized Z-score was computed as $\Delta Z_{\text{Drug}} = (Z_{\text{Drug}} - Z_{\text{DMSO}}) / \sqrt{2}$, with the variance corrected by the $\sqrt{2}$ factor. Homoscedasticity was assumed as variances are approximately the same across the treatments (Figure S1G). Synthetic sick/lethal interactions (under a given drug treatment) were defined by $\Delta Z_{\text{Drug}} < -2.4$, whereas buffering interactions were defined by $\Delta Z_{\text{Drug}} > 4.8$. Among buffering interactions, suppressors additionally satisfied the condition $Z_{\text{Drug}} > 2.4$, whereas the rest ($Z_{\text{Drug}} \geq 2.4$) were termed epistatic buffering. The two-sided p values for the Z-scores and normalized Z-score were calculated assuming the irrelevant genes follow a normal distribution with the same mean and variance as null distribution defined by the genes with lowest expression. To control for family-wise error rates for the p values, we computed false discovery rates (FDR) using the Benjamini-Hochberg (BH) approach (Benjamini, 1995)

To score each gene using MAGeCK (Li et al., 2014), normalized sgRNA read counts from the triplicates in each condition were used as input for MAGeCK v0.5.3 to obtain a p value and FDR for gene enrichment or depletion relative to the reference samples (day 15 DMSO) MAGeCK was run with default parameters. The smaller value between positive and negative modes is shown in Table S3.

Pathway Analysis

Gene set enrichment analysis (GSEA) (Mootha et al., 2003) was performed on the list ranked by ΔZ_{Drug} using default parameters. A customized geneset database containing all KEGG Metabolism or Cellular Process pathways (92 total) with 15-500 genes was used for the GSEA. The KEGG Oxidative Phosphorylation and Complex I pathways were manually reviewed. All pathways with GSEA FDR < 0.05 were considered significant.

Hierarchical Clustering

Mean log2 fold-change across sgRNAs was computed for each gene in each replicate and genes with low expression were filtered as described in the **Gene scoring** section. This gene set of 11,102 genes was further filtered such that only the top 10% genes with the largest variance across all samples were kept. The final gene set contains $\sim 1,100$ genes. The mean log2-fold changes across sgRNAs for genes were clustered with average linkage hierarchical clustering using Pearson correlation distance metrics. Hierarchical clustering was applied using SciPy 1.1.0. The MitoCarta2 human database was used for labeling known mitochondrial localized proteins (Calvo et al., 2016).

For gene function annotation, we downloaded GO terms for all genes from DAVID 6.8 (Huang da et al., 2009) for the GO_BP_DIRECT, GO_MF_DIRECT, and GO_CC_DIRECT annotations. For each node on the hierarchical clustering dendrogram, the hyper-geometric test p value was calculated for all GO terms. Nodes were highlighted as key nodes if they contained at least one GO term with $p < 10^{-10}$ and at least one term scoring higher than any other node. To reduce redundancy, a lower node was removed if the upper node contained more than 80% of its genes.

DATA AND CODE AVAILABILITY

All screening data generated during this study are provided as Supplemental Tables. Expression levels in K562 cells are based on RNaseq sample GSM854403 in GEO series GSE34740 (Slavoff et al., 2013). MATLAB and Python source codes are available at: <https://github.com/yangli88>.

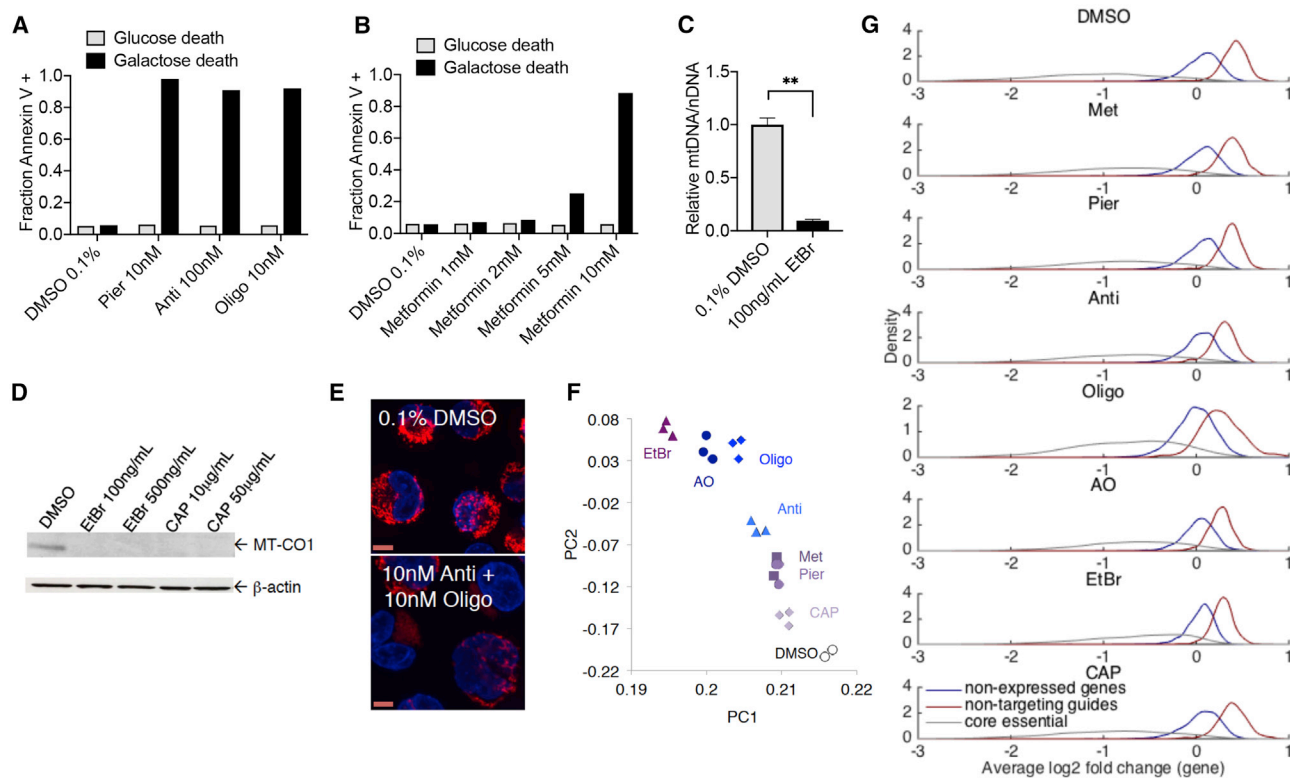


Figure S1. Additional Data, Related to Figure 1

(A) Cell death as assessed by Annexin V staining and flow cytometry in K562 cells cultured in glucose or galactose containing medium with the specified OXPPOS inhibitors.

(B) Cell death as assessed by Annexin V staining and flow cytometry in K562 cells cultured in glucose or galactose containing medium with different doses of metformin.

(C) Real time PCR-based measurement of mtDNA relative to nuclear DNA (nDNA) in K562 cells after 9 days of ethidium bromide treatment (average \pm SEM, $n = 3$ replicates from one experiment).

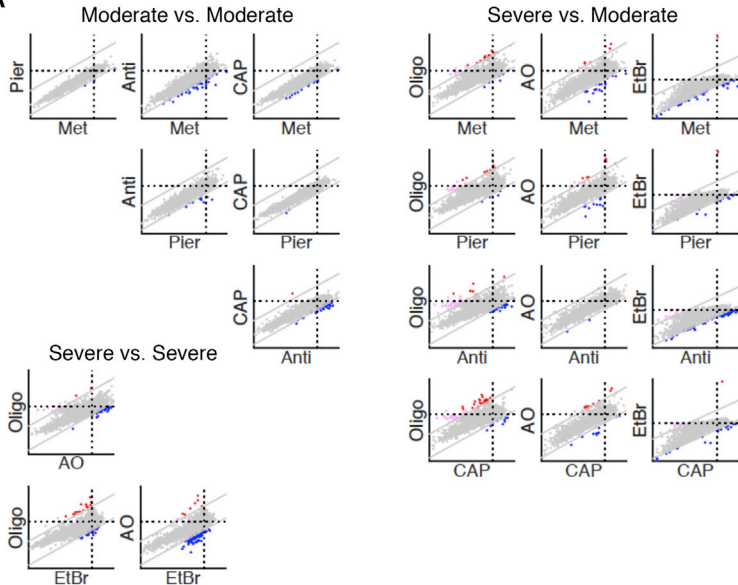
(D) Immunoblots for the mtDNA encoded MT-CO1 and loading control in K562 cells after 9 days of ethidium bromide (EtBr) or chloramphenicol (CAP) treatment.

(E) Membrane potential measurement by TMRM staining (red) and confocal microscopy in K562 cells after 3 days of antimycin+oligomycin treatment. Nuclei were stained with Hoechst 33342 (blue). Scale bar = 5 μ m.

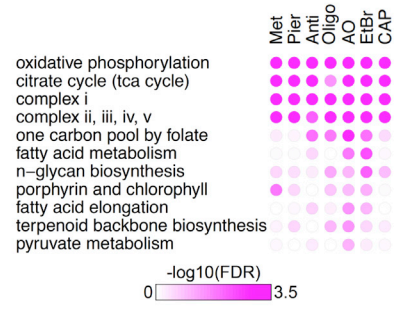
(F) Principal component analysis (PC1: 89%, PC2: 3%) on guide abundance on day 15 across all biological replicates.

(G) Histograms of average log₂ fold changes for all genes (between day 15 samples and day 0 baseline). The average log₂ fold change for each gene was calculated by taking the mean of its 4 sgRNAs. Biological triplicates were averaged by taking the mean. Shown are distributions for 3,726 non-expressed genes in K562 (dark blue), 1,000 non-targeting sgRNAs (maroon), and the core essential genes as defined in (Hart et al., 2015) (gray).

A



B



C

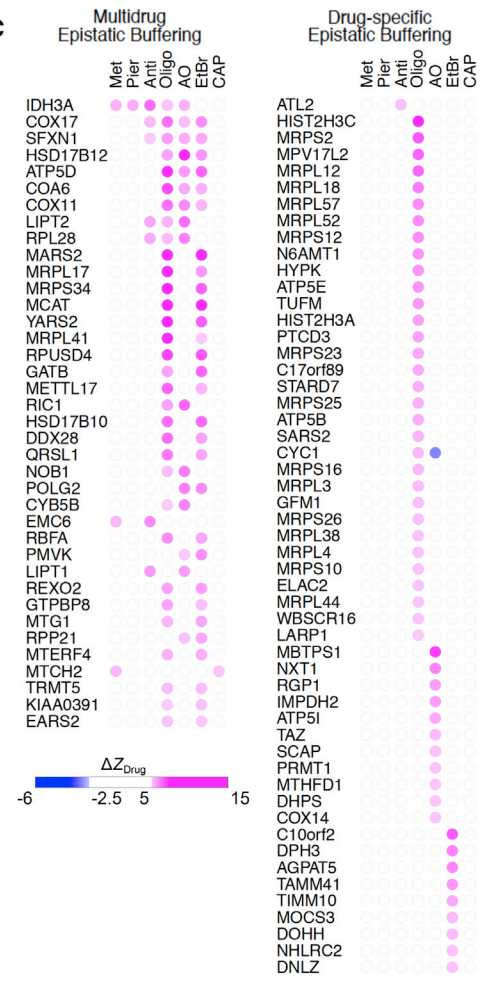


Figure S2. Additional Data, Related to Figure 2

(A) Scatterplots of Z-scores showing knockouts (KOs) that are enriched or depleted in each pairwise drug versus drug comparison. Axis label denotes the Z-score of the specified drug. KOs are scored by $\Delta Z_{\text{Drug-Drug}} = (Z_{\text{Drug}, y \text{ axis}} - Z_{\text{Drug}, x \text{ axis}}) / \sqrt{2}$. Enrichment (shown in red or magenta, $\Delta Z_{\text{Drug-Drug}} > 4.8$) and depletion (shown in blue, $\Delta Z_{\text{Drug-Drug}} < -2.4$) are used to define drug-specific buffering and synthetic sick/lethal interactions, respectively. Among buffering interactions, drug-specific suppressors ($Z_{\text{Drug}, y \text{ axis}} > 2.4$) are shown in red. Scatterplots are grouped based on the impact of drug treatment on proliferation (moderate or severe), according to the growth curves shown in Figure 1C. The gray dotted lines represent the cutoffs for drug-specific interactions.

(B) Top categories of KEGG pathways among enriched KOs by Gene Set Enrichment Analysis (GSEA). The 11,102 genes was ranked by ΔZ_{Drug} in descending order and GSEA was run in the positive mode. Pathways are ordered by the maximum of $-\log_{10}$ FDR across 7 drugs.

(C) The 91 genes involved in epistatic buffering interactions that score in ≥ 1 drug ($\Delta Z_{\text{Drug}} > 4.8$, and $Z_{\text{Drug}} \leq 2.4$). Genes are further divided into two panels. The left panel contains genes that have interactions with multiple drugs, and is ordered by the number of drugs under which interactions occur. The right panel contains genes with only drug-specific interactions, and genes are listed by the specific drug and ordered by the strength of interaction. Gene-drug pairs that do not score are colored white ($-2.4 \leq \Delta Z_{\text{Drug}} \leq 4.8$).

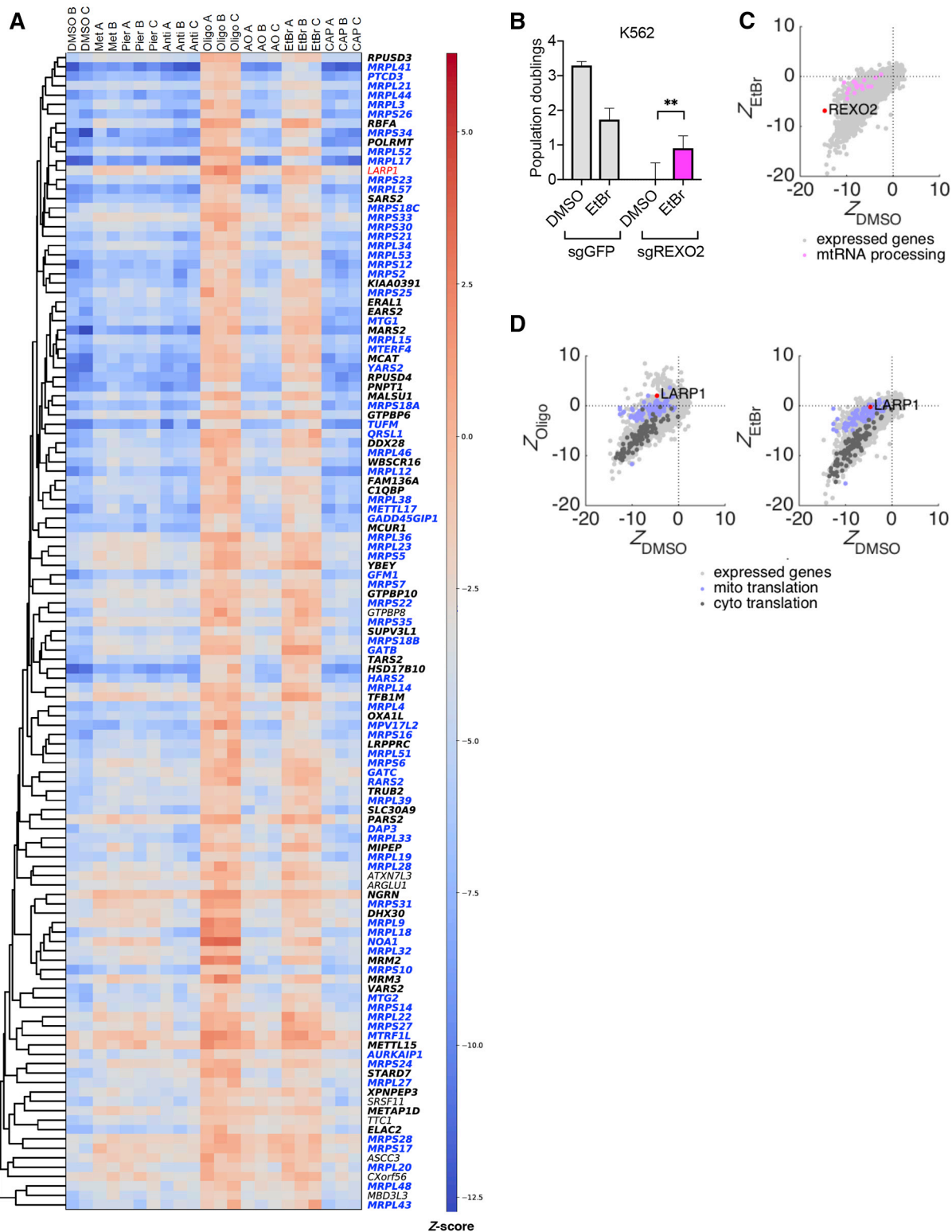


Figure S4. Additional Data, Related to Figure 5

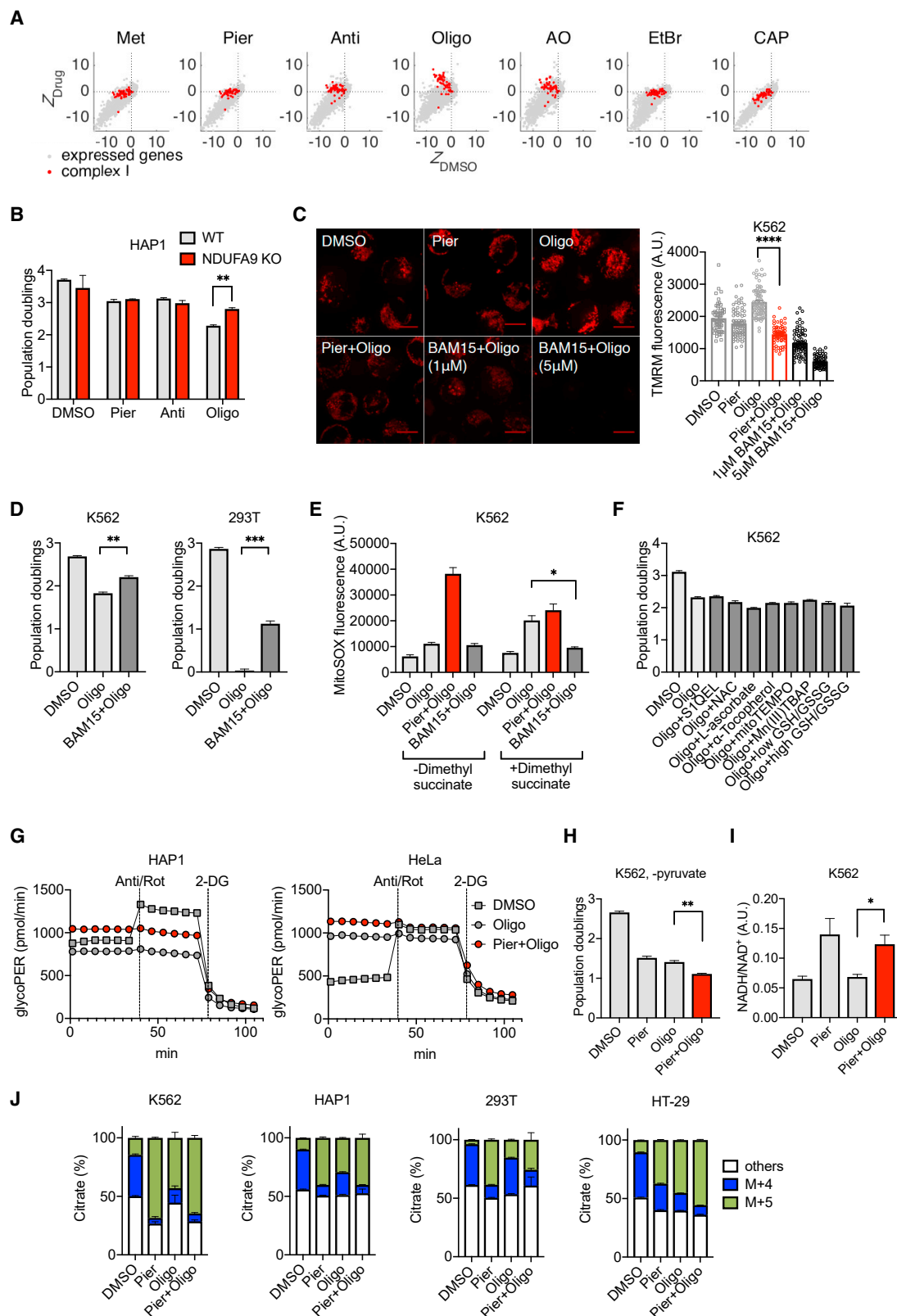
(A) Clustergram of a gene module within “Mitochondrial translation” in Figure 5D. *LARP1* is labeled with a red. Genes involved in mitochondrial translation by GO annotations are labeled blue. Genes currently listed in the MitoCarta2.0 (Calvo et al., 2016) database are boldfaced.

(legend continued on next page)

(B) Validation of the buffering interaction between *REXO2* loss and ethidium bromide in K562. Cell counts were performed 3 days post 10 ng/mL ethidium bromide treatment (average \pm SEM, n = 3). **<0.01 indicates two-tailed Student's t test p value.

(C) Scatterplot of Z-scores highlighting KO of *REXO2* in ethidium bromide versus DMSO. Genes involved in mtRNA processing are highlighted magenta.

(D) Scatterplots of Z-scores highlighting KO of LARP1 in oligomycin (left panel) or ethidium bromide (right panel) versus DMSO. Genes encoding for mitochondrial ribosomes or tRNA synthetases are highlighted purple, whereas genes encoding for cytosolic ribosomes or tRNA synthetases are highlighted dark gray.



(legend on next page)

Figure S5. Additional Data, Related to Figure 6

(A) Scatterplot of the fitness of a gene KO in the specified drug (Z_{Drug}) versus fitness in DMSO (Z_{DMSO}). Gray dots denote all 11,102 genes in the analysis and the red dots denote 50 nuclear genes that encode structural subunits and assembly factors of complex I.

(B) Drug specificity in genetic suppression by *NDUFA9* loss in HAP1 cells. Cell counts were performed 3 days post drug treatment (average \pm SEM, $n = 2$).

(C) Membrane potential measurement by TMRM staining (red) and confocal microscopy in K562 cells after the specified treatment. Scale bar = 5 μ m. Right: Quantification of TMRM in individual cells using the maximum intensity. **** <0.0001 indicates two-tailed Student's t test p value.

(D) Validation of BAM15 at 1 μ M as suppressor of oligomycin in K562 and 293T cells. Cell counts were performed 3 days post drug treatment (average \pm SEM, $n = 3$). ** <0.01 or *** <0.001 indicates two-tailed Student's t test p value.

(E) Mitochondrial superoxide measurement by mitoSOX staining and flow cytometry in K562 cells after the specified drug treatment. Dimethyl succinate was used at 5 mM and BAM15 was used at 1 μ M. * <0.05 indicates two-tailed Student's t test p value.

(F) Growth phenotypes of cells under a combination of oligomycin and known antioxidants in K562: S1QEL (10 μ M), NAC (2 mM), L-ascorbate (10 μ M), α -Tocopherol (100 μ M), mitoTEMPO (100 μ M), Mn(III)TBAP (100 μ M), low GSH/GSSG (10 μ M/1 mM), and high GSH/GSSH (1 mM/10 μ M). Cell counts were performed 3 days post drug treatment (average \pm SEM, $n = 3$).

(G) Corrected extracellular acidification rate as assessed by the Seahorse Extracellular Flux (XFe96) Analyzer in HAP1 and HeLa after 3 days of drug treatment (average \pm SEM, $n = 12$).

(H) Growth phenotypes of cells under a combination of piericidin and oligomycin in K562 in the absence of 1 mM pyruvate supplementation. Dialyzed serum was used. Cell counts were performed 3 days post drug treatment (average \pm SEM, $n = 3$). ** $p < 0.01$ indicates two-tailed Student's t test p value.

(I) Ratio of whole cell NADH to NAD⁺ levels in K562 using targeted mass spectrometry after 3 days of drug treatment (average \pm SEM, $n = 3$). * $p < 0.05$ indicates two-tailed Student's t test p value.

(J) The ¹³C labeling pattern of citrate over the course of 8 h upon supplementation with [U-¹³C]glutamine in K562, HAP1, 293T, and HT-29 (average \pm SEM, $n = 3$).